ACCSCIENCE PUBLISHING

International Journal of Bioprinting

RESEARCH ARTICLE

# Effect of seed distribution characteristics on mechanical properties, degradation behavior, and osteogenic differentiation of additively manufactured Voronoi-based biomimetic scaffolds

**Boxun Liu[1,2], Yunhui Wang[1,2], Yushan Huang[2], Zhi Dong[2], Yi Zhang[1], Zhengbo Wen[1], QiXin Liang[1], and Changjun Han[2*]**

[1] Huamei (Shenzhen) BioTech Co., Ltd, Shenzhen, Guangdong, China

[2] School of Mechanical and Automotive Engineering, South China University of Technology, Guangzhou, Guangdong, China

***Corresponding author:**
Changjun Han
(cjhan@scut.edu.cn)

**Citation:** Liu B, Wang Y, Huang Y, *et al*. Effect of seed distribution characteristics on mechanical properties, degradation behavior, and osteogenic differentiation of additively manufactured Voronoi-based biomimetic scaffolds. *Int J Bioprint*. 2026;12(1):500-522. doi: 10.36922/IJB025450466

**Received:** November 4, 2025
**Revised:** December 7, 2025
**Accepted:** December 9, 2025
**Published online:** December 18, 2025

## Abstract

The application of bionic porous structures based on Voronoi diagrams in bone defect repair has been extensively studied, with seed distribution characteristics recognized as key parameters affecting the performance of Voronoi scaffolds. In this study, a controllable parametric design method for Voronoi scaffolds was employed to experimentally and numerically investigate the effects of seed count and porosity on the mechanical properties, degradation behavior, mass transfer efficiency, and cell activity of laser powder bed fusion–printed degradable zinc-based Voronoi bone scaffolds. The results revealed the influence mechanisms of seed distribution characteristics on the mechanical properties and deformation modes of Voronoi scaffolds, achieving a 26.9% enhancement in failure stress. Moreover, by adjusting seed distribution, the degradation rate was precisely regulated within the range of 0.027–0.157 mm/year, enabling a 5.8-fold control over the release of zinc ion. Additionally, the effect of seed density on the osteogenic performance and gene expression of mouse pre-osteoblast cells were examined, demonstrating that higher seed densities predominantly upregulated *COL1* and *ALP* expression to promote osteogenic differentiation. Increasing the seed count density elevated *COL1* expression to 4.5 times that of the control group. These findings provide a theoretical basis for the clinical application and performance optimization of degradable zinc-based Voronoi bionic bone scaffolds.

***Keywords:*** Additive manufacturing; Cell activity; Degradation behavior; Laser powder bed fusion; Seed density; Voronoi scaffold

## 1. Introduction

Metal bionic bone scaffolds manufactured via laser powder bed fusion (LPBF) technology feature complex and fine internal bionic architectures,[1,2] with highly interconnected pores that closely mimic the natural morphology of human bone tissue.[3-5] These porous scaffolds not only provide mechanical support but also offer design flexibility to regulate structural parameters for enhancing cell adhesion, proliferation, and differentiation.[6] During the design phase, various biocompatible metal materials, such as titanium alloys, 316L stainless steel, cobalt-chromium alloys, and zinc alloy, can be selected to meet the specific performance requirements of different anatomical sites.[7-9] In addition, computer-aided design tools enable patient-specific customization of metal bone scaffolds, facilitating clinical applications, such as craniofacial defect repair and interbody fusion cage implantation.[10-12] Despite significant progress in repairing site-specific bone defects, the biological and structural complexity of cancellous bone poses a major challenge in developing truly biomimetic implants. As an essential internal scaffold within the skeletal system, cancellous bone provides critical mechanical support and energy absorption, contributing to bone tissue development and overall biomechanical functionality.[13-14] However, its complex three-dimensional (3D) porous architecture makes it difficult to replicate using conventional manufacturing techniques.[15] Therefore, there is an urgent need with high structural fidelity to native cancellous bone and matched biomechanical performance.

To achieve LPBF-printed scaffolds with structural and mechanical properties closely matching those of cancellous bone, it is necessary to investigate and design based on elemental structural characteristics. Traditional designs employ periodic lattice porous configurations,[16] such as body-centered cubic (BCC) and face-centered cubic (FCC), which are constructed through uniform struts connected at regular nodes. These lattice configurations, often inspired by atomic crystal arrangements, offer advantages in weight reduction and enhanced energy absorption while maintaining mechanical strength.[17] However, their inherent regularity limits the ability to replicate the stochastic pore architecture of cancellous bone. To address this limitation, biomimetic approaches have gained increasing attention in bone implant design.[18-19] Among these, Voronoi diagrams, which are computational geometric segmentation based on seed point distribution,[20] applied in materials science, biology, and medicine.[21] Fantini and Curto[22] introduced a bioinspired structural generation method utilizing Voronoi tessellation, demonstrating that Voronoi-based porous architectures can effectively mimic the morphological features of natural trabecular bone. Moreover, such scaffolds exhibited excellent geometric adaptability to complex bone defect contours and ensured mechanical continuity, making them highly promising for medical implant applications.[23-24] Zhao *et al.*[25] further developed an optimized Voronoi-based design approach, showing that irregular porous structures derived from Voronoi segmentation exhibited superior structural stability compared to traditional regular lattices. Additionally, they achieved gradient scaffolds with tunable mechanical properties that closely matched the Young's modulus of natural bone, providing a theoretical basis for designing functionally graded irregular porous scaffolds. Gómez *et al.*[26] employed Voronoi segmentation to construct a porous model with virtual isotropy, which demonstrated highly consistency with key bi-morphological parameters of trabecular bone and enabled precise regulation of structural properties during the preliminary stages of microstructural design and histomorphometric analysis. In summary, biomimetic bone implant designs based on the Voronoi principle can accurately replicate the irregular microarchitecture of natural bone,[27] achieve close alignment with trabecular morphometric parameters through parametric control,[28] and thus show significant potential for application in bone tissue engineering and biomedical implants.[29-33]

Currently, numerous studies have integrated Voronoi-based biomimetic bone implants with LPBF. However, research on LPBF-printed Voronoi metallic bone scaffolds primarily focuses on the influences of process parameters, such as laser power, scanning speed, scanning strategy, and porosity, on the printing quality and mechanical properties of these scaffolds.[34-38] For example, Hou *et al.*[39] studied how different laser parameters and scanning strategies affected the geometric accuracy and internal defect formation in Ti6Al4V Voronoi scaffolds printed by LPBF. Their findings demonstrated that optimizing LPBF process parameters could significantly enhance the structural fidelity of Voronoi architectures. He *et al.*[40] developed a biomimetic scaffold featurin1g a Voronoi-graded pore distribution, achieving favorable mechanical performance by regional porosity control. The resulting Young's modulus and ultimate strength range ranged from 1.50 to 7.12 GPa and 38.55 to 268.03 MPa, respectively. Despite these advances, limited attention has been paid to the seed configuration in Voronoi scaffolds. As a critical design parameter, seeds directly determine the average pore size and the stochastic strut distribution morphology of Voronoi scaffolds,[41-46] which are crucial for tailoring bionic bone scaffolds to meet site-specific clinical requirements. Furthermore, recent work has demonstrated the fabrication of Voronoi metamaterials with lattice-inspired topologies using LPBF, showing that such design strategy based on modified seed distributions can generate periodically arranged architectures with improved mechanical properties.[47] Therefore, the seeds play an important role in determining the performance of Voronoi scaffolds printed by LPBF.[48-50] There remain gaps in the research on the degradation and biological performance of LPBF-printed Voronoi scaffolds with the variation of seed control. Moreover, the combined effects of seed distribution and porosity on the structural properties (i.e., mechanical properties, degradation behavior, mass transfer efficiency, and cell viability) of Voronoi scaffolds have not been systematically investigated.

Therefore, the work primarily studied the effects of seed distribution characteristics on the mechanical properties, degradation ability, mass transfer efficiency, and osteogenic differentiation of zinc-based Voronoi bone scaffolds printed by LPBF. Specifically, Voronoi scaffold models with varying seed counts and densities as well as porosities were designed. The mechanical properties, deformation mechanisms, and failure modes of these scaffolds were analyzed through a combination of experimental testing and finite element simulations. The degradation behavior, mass transfer efficiency, and cell responses of the LPBF-printed zinc-based Voronoi scaffolds were evaluated by adjusting porosity and seed distributions. The findings can provide a valuable insight to the biomimetic design of biodegradable Voronoi-based scaffolds for trabecular bone implant applications.

## 2. Materials and methods

### 2.1. Design of Voronoi-based biomimetic scaffolds

The Voronoi diagram is defined as follows, given a set of discrete seeds of number $k$ ($k > 1$) in an $m$-dimensional Euclidean space[51]:

$$P = \{p_1, \ldots, p_k\} \in R^m \tag{I}$$

where $m$ represents the dimensionality of the space, $R$ denotes the $m$-dimensional Euclidean space, $p_k$ is the $i$th seed ($i = 1, \ldots, k$); and $P$ denotes the set of all seeds. In the 2D plane, the boundaries of the Voronoi diagram consist of vertical bisectors between adjacent seeds. In 3D space, the separating surfaces of Voronoi cells are formed by the intersection of spheres centered at neighboring seeds. For each seed $p_i$, the corresponding Voronoi cell $V(P_i)$ consists of all points in space whose distance to $p_i$ is less than or equal to the distance to any other seed $p_j$ ($j \neq i$). The Voronoi cell can be formally defined by the following mathematical expression

$$V(p_i) = \{p | d(p, p_i) \le d(p, p_j), j \neq i, j = 1, \ldots, n\}. \tag{II}$$

Here, $p_i$-$p_n$ denotes a finite set of seeds located in the geometric domain, and $d(p, p_i)$ represents the Euclidean distance between a point $p$ and the seed $p_i$.

The design procedure of the Voronoi biomimetic scaffolds is illustrated in Figure 1. In 3D space, the boundaries of the Voronoi cells were formed through the expansion and mutual contact of spheres centered at the

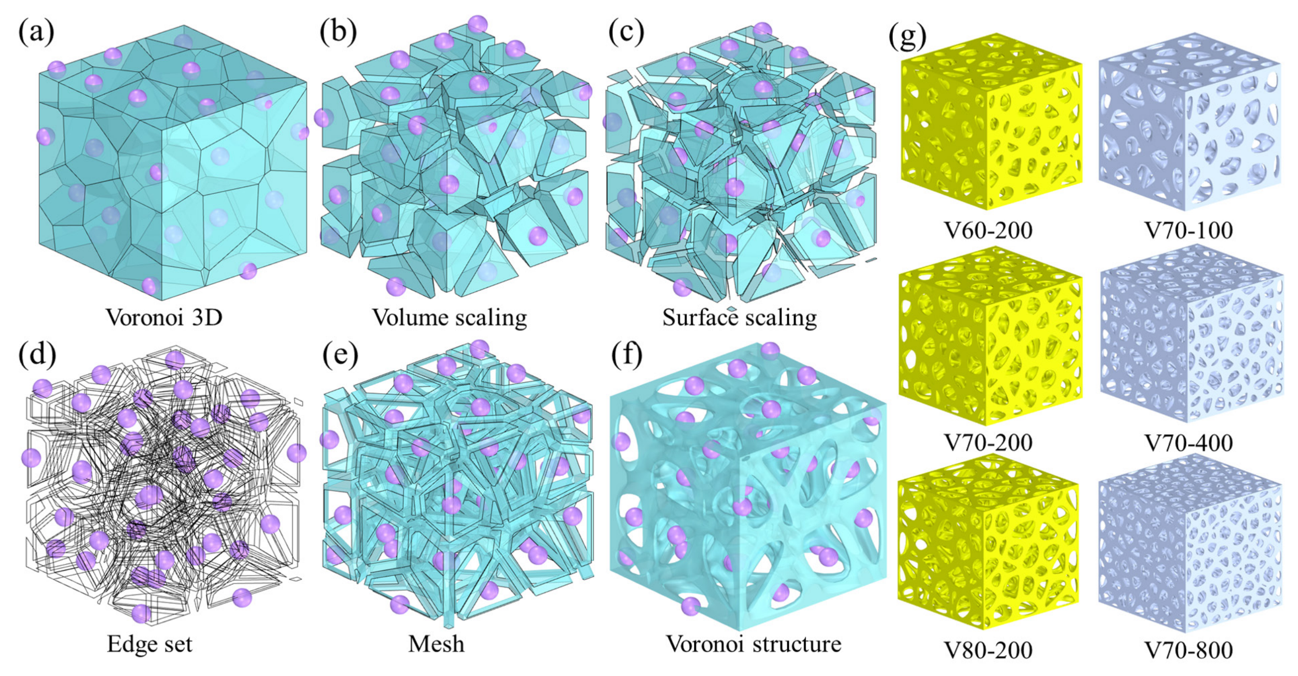

**Figure 1.** Design procedures of Voronoi biomimetic scaffolds. (a) Voronoi 3D. (b) Cell face scaling. (c) Cell body scaling, (d) Edge line extraction. (e) Mesh extraction. (f) Voronoi biomimetic scaffold construction. (g) 3D models with different seed counts and porosities.

seeds; the Voronoi cells were defined by the perpendicular bisecting surfaces connecting adjacent seeds. To achieve strut morphologies with high connectivity, large specific surface area, and structural similarity to bone trabeculae, the pore volume of the bionic structure was generated by hollowing out the Voronoi cells and enabling inter-pore penetration through shared faces. First, Voronoi cells were constructed via Delaunay triangulation based on the seed set *P* and boundary constrains. Each resulting Voronoi cell served as a pore precursor in the porous structure. Subsequently, volumetric and facial elements of the Voronoi polygons were uniformly scaled using scaling coefficients *Sv* and *Sf* (Figure 1b and c), yielding the edge network of the Voronoi bionic scaffold (Figure 1d). A mesh was then generated based on the mapping relationship of these edges, defining the solid–pore interface of the structure (Figure 1e). Finally, postprocessing of the boundary surface mesh produced the completed Voronoi scaffold (Figure 1f).

To achieve parametric control in the design of Voronoi scaffolds, the mathematical relationships among structural porosity *u*, seed count *n*, average pore diameter $d_m$, and the design parameters *Sv* and *Sf* were established. The internal pores of the scaffold were approximated by scaled Voronoi cells. The volume of the ith pore ($i = 1, ..., n$) in the Voronoi-based trabecular bone scaffold was approximated by the volume $V(P_i)$ of the corresponding scaled Voronoi cell. An approximately proportional relationship existed between the porosity u of the Voronoi scaffold and the scaling factor *Sv*, expressed as

$$u \approx S_v . \tag{III}$$

The derivation of the formula proceeded as follows: $V(C_i)$ denotes the volume of the ith ($i = 1, ..., n$) unscaled Voronoi cell, and *n* represents both the spatial seed count and the number of corresponding Voronoi polygons. The total spatial volume within the geometric boundary is then given by

$$V_{box} = \sum_{i=1}^{n} V(C_i) . \tag{IV}$$

The volume of the porous part, scaling factor, and porosity can be respectively expressed by

$$V_P \approx \sum_{i=1}^{n} V\left(P_i\right), \tag{V}$$

$$S_v = \frac{\sum_{i=1}^{n} V\left(P_i\right)}{\sum_{i=1}^{n} V\left(C_i\right)} = \frac{V_P}{V_{\text{box}}} , \tag{VI}$$

$$u \approx \frac{V_P}{V_{\text{box}}} = S_v . \tag{VII}$$

Based on this, the pore volume $V(P_i)$ in the Voronoi scaffold is approximated as a sphere for calculation. Consequently, under constant porosity, a relationship between the number of spatial seeds *n* and the average pore diameter $d_m$ can be established as follows

$$n = \frac{u * V_{\text{box}}}{\frac{4}{3}\pi(\frac{d_m}{2})^3} = \frac{6u * V_{\text{box}}}{\pi d_m{}^3} . \tag{VIII}$$

The higher porosity of cancellous bone endows it with characteristics, such as low density, a reduced Young's modulus, and a large surface area. These properties not only facilitate mechanical load transmission while providing sufficient space for bone tissue attachment and growth, but also enhance the diffusion of nutrients and metabolic waste. Cancellous bone typically exhibits porosity exceeding 50%. To ensure compatibility between implant porosity and native bone, square Voronoi models (10 × 10 × 10 mm$^3$) with porosities of 60%, 70%, and 80%—generated using 200 seeds (hereafter referred to as V60-200, V70-200, and V80-200, respectively)—were used to study the influence of porosity on the performance of Voronoi biomimetic scaffolds. These models exhibited average pore diameters of 2.37, 1.49, and 1.18 mm, respectively. In addition, to examine the effect of seed density—and consequently average pore diameter—on structural performance at a constant material volume fraction, Voronoi scaffold models incorporating 100, 400, and 800 seeds were analyzed. These models yielded average pore diameters of 1.97, 1.88, and 1.79 mm, respectively, within a consistent 10 × 10 × 10 mm$^3$ cubic dimensions and a fixed porosity of 70% (hereafter denoted as V70-100, V70-400, and V70-800). All scaffold models are presented in Figure 1g.

### 2.2. Material and LPBF process

The LPBF process used atomized zinc powder exhibiting a smooth surface and high sphericity, with only a minor presence of satellite particles, as observed using scanning electron microscopy (SEM; FEI Nova nano 430, Netherlands) (Figure 2a). Particle size distribution was analyzed using a laser particle size analyzer (LPSA;

Microtrac S3500), revealing an average particle diameter of 10.9 μm and an overall normal distribution pattern (Figure 2b). The processing parameters included a laser spot diameter of 70 μm, a laser power of 80 W, a scanning speed of 600 mm/s, a hatch spacing of 55 μm, a layer thickness of 30 μm, and a scanning direction rotated by 45° between consecutive layers. The LPBF-printed Voronoi-based zinc scaffolds with different seed distributions and porosities are shown in Figure 2c. The sample porosity was determined based on the Archimedes displacement method.

### 2.3. Quasistatic compressive testing and FEM simulation

The compressive performance of LPBF-printed Voronoi scaffolds was evaluated using a CMT5105 universal testing machine (SANS Experimental Equipment Co., Ltd, China). Prior to testing, the scaffold samples were subjected to ultrasonical cleaning to remove residual powder and cutting fluid adhering inside the structural pores. The compression termination displacement was set at 60% of the sample height. The compressive stress–strain curve was derived by converting the recorded force–displacement curve data. Three replicate samples were tested for each parameter and configuration of the Voronoi scaffolds, and the average response was taken to represent the compressive performance under the given condition. The energy absorption (*EA*) of the printed Voronoi scaffolds was calculated by integrating the area under the force–displacement curve, as described by

$$EA(d) = \int_0^d F(x)\,dx, \qquad \text{(IX)}$$

where $d$ represents the compression displacement. To comprehensively evaluate the energy absorption capacity of the samples under different porosities, specific energy

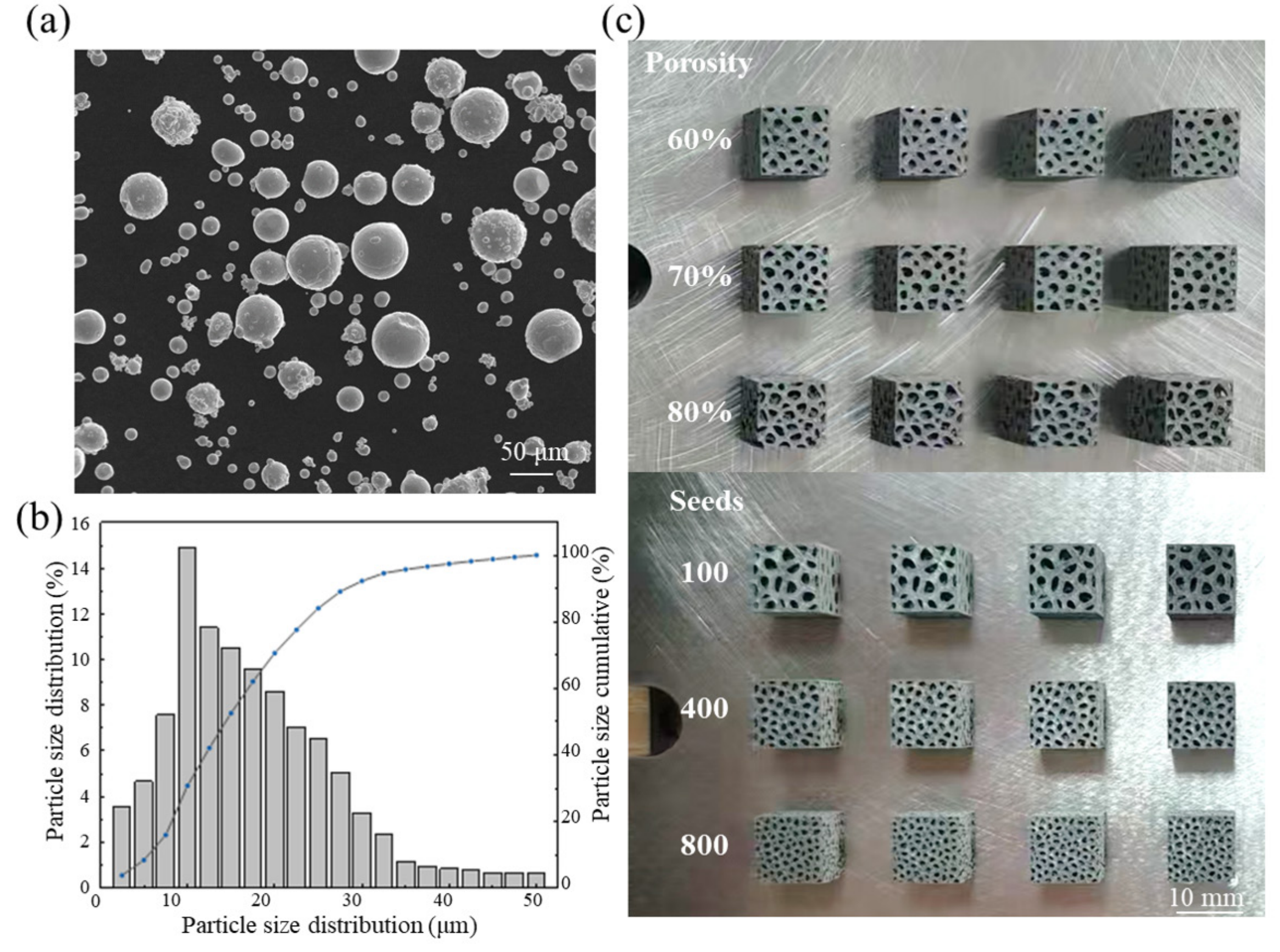

**Figure 2.** Characteristics of zinc powder and the zinc-based Voronoi scaffolds printed via LPBF (a) Morphology of zinc powder. (b) Particle size distribution of zinc powder. (c) LPBF-printed Voronoi scaffolds with different porosities and seed counts. Abbreviation: LPBF, Laser powder bed fusion.

absorption (*SEA*) is used to quantify the energy absorption performance per unit mass. The calculation method is as follows

$$SEA(d) = \frac{EA(d)}{m}, \tag{X}$$

where $m$ represents the mass of the scaffold. The finite element method (FEM) simulation model consisted of a compression plate, a fixed plate, and a Voronoi scaffold. The Voronoi scaffold was positioned on the fixed plate and subjected to loading from the compression plate. Both the compression and fixed plates were assigned reference points and defined as rigid bodies. A surface-to-surface contact interaction was established between each plate and the Voronoi scaffold to accurately capture interfacial behavior. An explicit dynamic solver was employed, along with an elastoplastic hardening material model. The Voronoi scaffold was discretized using C3D10M (modified 10-node quadratic tetrahedral elements) with a mesh feature size of 0.3 mm. Material properties were derived from the tensile stress–strain response of LPBF-printed zinc,[52-53] with the following parameters: density of $7.16 \times 10^{-9}$ t/mm$^3$, Young's modulus of 93.16 GPa, yield strength of 93.71 MPa, and tensile fracture strain of 11.17%. To ensure the accuracy of the results, the ratio of kinetic energy to internal energy was maintained below 5%.

### 2.4. Computational fluid dynamics simulation

The permeability of the biomimetic bone scaffold plays a critical role in facilitating the transport of nutrients and metabolic products, as well as influencing cell adhesion and proliferation. To evaluate its capability of effective mass transport, a computational fluid dynamics (CFD) model was developed based on continuum mechanics and mass transfer principles using COMSOL Multiphysics (COMSOL Inc., Sweden), enabling the simulation of fluid flow under laminar conditions. By applying the conservation of momentum, the Navier–Stokes equations were used to describe the mass transport behavior of viscous, incompressible fluids within the continuous fluid domain, as expressed by

$$\rho \frac{DV}{Dt} = \rho f - \nabla p + \mu \nabla^2 V \tag{XI}$$

where $\rho$ represents the fluid density; $\frac{DV}{Dt}$ denotes the guiding number; $V$ is the velocity vector of the fluid; $f$ represents the noncontact volumetric force applied to the fluid; $\nabla$, $p$, and $\mu$ represent the Hamiltonian operator, pressure, and dynamic viscosity, respectively. Based on this, the permeability of the Voronoi scaffold and its relationship with the pressure gradient are determined using Darcy's law

$$k = Q\mu L / A\Delta P, \tag{XII}$$

where $k$ represents the permeability; $Q$ represents the volumetric flow rate; $L$ represents the length of the Voronoi scaffold along the fluid flow direction; $A$ represents the cross-sectional area of the model; and $\Delta P$ is the pressure drop between the inlet surface and the outlet surface. A square region with a cross-sectional area of 10 × 10 mm² and a height of 15 mm was defined to perform Boolean cutting on the Voronoi model, thereby constructing the fluid domain for CFD simulation. The fluid entered though the top surface inlet in the negative Z direction at a constant velocity of 1.0 mm/s, simulating typical human body fluid flow rates.[54] During the simulation of the pressure drop and velocity distribution, the inlet speed was maintained constant, the outlet pressure was set to zero, and the four lateral surfaces perpendicular to the xy-plane were designated as wall boundary planes. The working fluid was deionized water, with a density of 1,000 kg/m$^3$ and a viscosity of $1.01 \times 10^{-3}$ Pa·s. To balance computational accuracy and efficiency, the fluid domain was discretized into tetrahedral elements with a nominal edge length of 0.3 mm.

Finally, the Reynolds number was calculated to determine whether the flow regime was laminar, thus evaluating the applicability of Darcy's law. The formula is given as

$$Re = \rho v l / \mu \tag{XIII}$$

where $v$ represents the velocity of the inlet surface, and $l$ represents the characteristic length. The simulation results indicated that all computed Reynolds numbers were below 10, verifying the validity of Darcy's law under the studied conditions.

### 2.5. Degradation behavior

This degradation experiment simulates the human physiological environment by conducting an *in vitro* degradation test of the zinc-based Voronoi scaffold in accordance with the ASTM-G31-72 standard.[55] The degradation process was carried out in simulated body fluid (SBF) with an initial pH of 7.4. Before weighing, the samples were ultrasonically cleaned and then dried in an oven at 50 °C for 1 h. After drying, the initial mass of each sample was measured using an electronic balance and recorded as $M_0$ (g). The SBF volume was determined based on a ratio of 10 mL/1 mm$^2$ of sample surface area (mm$^2$: mL = 10:1). All samples were placed in test tubes containing the SBF solution and immersed in a constant-temperature water bath maintained at 37 °C. Following 28 days of *in vitro* degradation, the samples were removed and slowly rinsed with deionized water to remove surface residues, and dried again at 50 °C for 1 h. The morphology of degradation products, including the corrosion layer formed on the sample surfaces, was analyzed using SEM. Subsequently, a corrosion solution was used to remove residual degradation products for accurate weight loss measurement. The corrosion solution was prepared by mixing 10 g of $CrO_3$, 16 mL of $AgNO_3$, and 34 mL of deionized water. After thorough cleaning, the samples were dried at 50 °C for 1 h, and their final mass $M_1$ (g) was recorded. Each sample group was tested in triplicate to ensure reproducibility. The degradation rate of the zinc-based Voronoi scaffold can be calculated according to the following formula

$$D_v = 8.76\times10^4 * \frac{M_0 - M_1}{\rho * \mathrm{A} * t}, \qquad \text{(XIV)}$$

where $D_v$ represents the degradation rate (mm/year), $\rho$ is the density of Zn, $A$ indicates the initial surface area of the sample (cm²), and $t$ represents the degradation time (hours).

### 2.6. Osteogenic performance and gene expression testing

The osteogenic performance and gene expression of the scaffolds were evaluated using mouse osteogenic precursor cells (MC3T3-E1). The Voronoi scaffolds were sterilized by ultraviolet irradiation and then immersed in Dulbecco's Modified Eagle Medium (DMEM) supplemented with 10% fetal bovine serum. Following incubation at 37°C for 72 h, the supernatant was collected to prepare a 100% extract, which was then diluted to 10% extract for experiments. The osteoinductive potential of the scaffolds was assessed by measuring alkaline phosphatase (ALP) activity and calcium nodule formation. MC3T3-E1 cells were seeded at a density of 4 × 10$^4$ cells per well in 24-well plates and cultured in medium containing 10% extract from different scaffold groups. After 7 and 14 days of culture, ALP activity was determined using an alkaline phosphatase assay kit (Beyotime, China), while calcium deposition was visualized using Alizarin red staining (ARS) (200 µL, Beyotime, China). Stained samples were imaged under a microscope (IX73, Olympus, Japan) to assess *in vitro* osteogenic differentiation. For quantitative real-time polymerase chain reaction (qRT-PCR) analysis, MC3T3-E1 cells were cultured under identical conditions for 7 and 14 days. Total RNA was extracted using Trizol reagent (Thermo Fisher Scientific, USA), and RNA concentration was quantified using a Nanodrop microplate spectrophotometer (Colibri, Titertek, USA) to evaluate gene expression levels. Sequences of primers used are shown in Table S1.

## 3. Results and discussion

### 3.1. LPBF printability

Table 1 presents the designed and experimental porosity values of the LPBF-printed Voronoi scaffolds. The experimental porosity was slightly lower than the designed value, primarily due to powder bonding during the LPBF process, which increased the thickness of struts. When seed count increased and seed density rose, the deviation between experimental and designed porosity became more pronounced. This trend could be attributed to the higher specific surface area associated with denser pore number, which intensified powder adhesion and fusion. Figure 3 displays the SEM images of the upper surfaces of Voronoi scaffolds with varying porosities and seed densities. These images revealed pores resulting from evaporation and unmelted powder particles.[56-57] Given that zinc is a low-boiling-point material, the rapid heating from the Gaussian laser beam and the uneven energy distribution led to swift evaporation of zinc within the molten pool. This generated turbulent vapor flow that

**Table 1. Porosity of LPBF-printed Voronoi scaffolds with different seed density and porosity values.**

| Structural type | Design porosity (%) | Actual porosity (%) | Deviation (%) |
|---|---|---|---|
| V60-200 | 60 | 55.8 ± 0.5 | −4.2 |
| V70-200 | 70 | 65.6 ± 0.7 | −4.4 |
| V80-200 | 80 | 75.3 ± 0.3 | −4.7 |
| V70-100 | 70 | 65.1 ± 0.4 | −4.9 |
| V70-400 | 70 | 63.4 ± 0.4 | −6.6 |
| V70-800 | 70 | 63.3 ± 0.1 | −6.7 |

Abbreviation: LPBF, Laser powder bed fusion.

disrupted the molten pool dynamics and causes spattering. As the porosity increased, the strut volume decreased, reducing local heat dissipation efficiency and making the surface more susceptible to slagging. Moreover, as the seed density increased, the strut size decreased. Due to the thin arc features at strut boundaries, localized thermal stress accumulation caused slight warping of strut contours. Both higher porosity and greater seed counts reduced local strut sizes, thereby compromising the structural integrity and overall printing quality.

### 3.2. Simulation and experimental mechanical responses

Quasistatic uniaxial compression tests and finite element simulations were conducted to investigate the mechanical response characteristics of Voronoi scaffolds with different seed counts and porosities (Figure 4). The simulated stress–strain curves agreed with the experimental results, except for the V80-200 sample, where the simulation slightly overestimated the stress. This discrepancy may be attributed to the amplification of the LPBF-produced defects at the microscale. The mechanical response during the stress plateau stage varied significantly with the seed count used to generate the scaffolds. As depicted in Figure 4a, the stress–strain curve of the V70-100 sample showed large fluctuations and a low plateau stress value. In contrast, the V70-400 sample exhibited reduced fluctuation and maintained a relatively stable flow stress up to 50% compressive strain. Beyond this point, the scaffold entered the densification phase. The mechanical response of the V70-800 sample was similar to that of V70-400 (Figure 4c), with the minor difference that its plateau stress was slightly lower than the failure stress, and it transitioned into the densification stage earlier. Increasing seed density resulted in a smoother stress plateau during the plastic flow stage and enhanced structural resistance to compression during densification, thereby improving yield strength. Moreover, higher seed density caused the Voronoi scaffold to reach the failure stress at lower engineering strains. These mechanical response characteristics were directly governed by the internal pore distribution, which was determined by the seed generation process. Figure 4d–f shows the compressive stress–strain behavior of V60-200, V70-200 and V80-200 samples. During compression, the Voronoi scaffolds with 60% porosity initially underwent elastic deformation, transitioned into plastic deformation, and reached the peak stress at 10% strain, with certain struts entering the strain hardening stage. The flow stress then increased gradually, and upon reaching 20% strain,

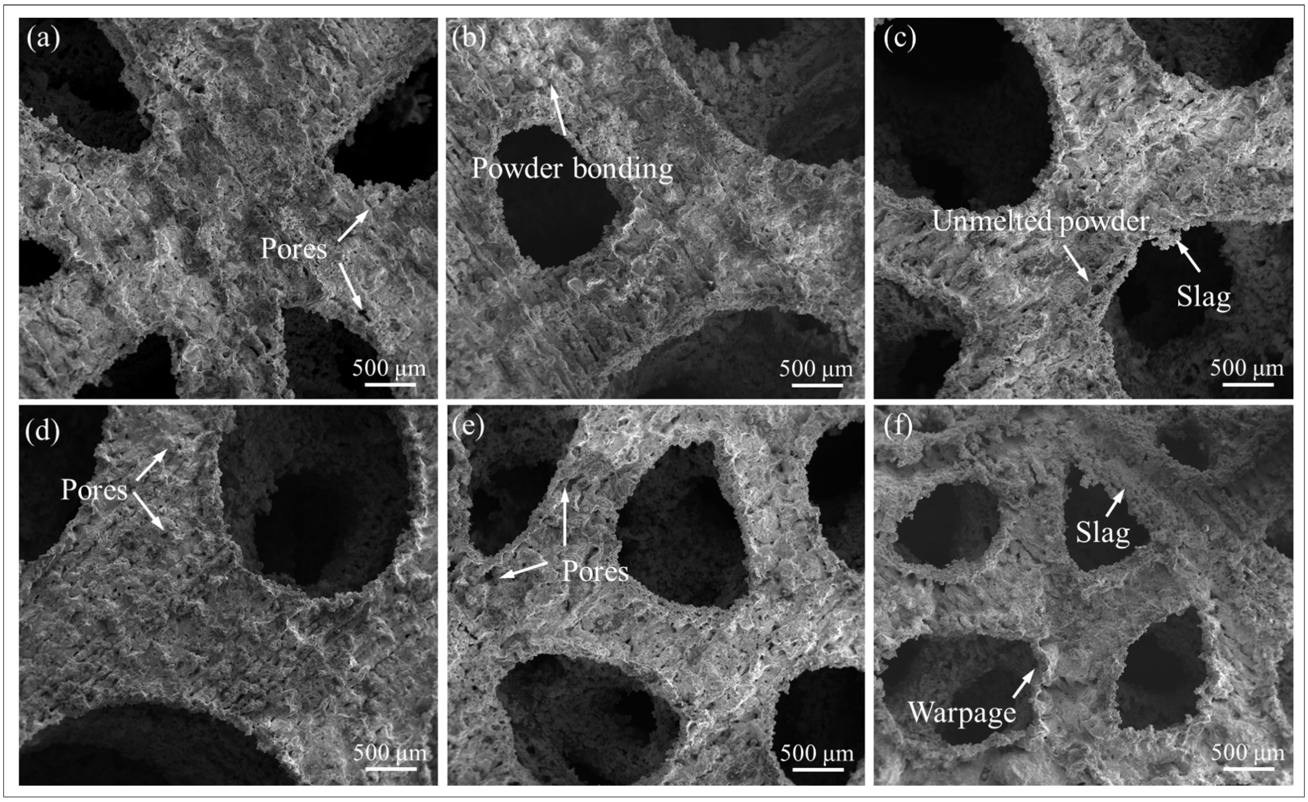

**Figure 3.** Surface morphology of Voronoi scaffold samples with different seed counts and porosities. (a) V60-200; (b) V70-200; (c) V70-200; (d) V70-100; (e) V70-400; (f) V70-800.

strut-to-strut contact and mutual compression-initiated densification, leading to an overall strain-hardening-typed response, and the stress–strain curve continued to rise (Figure 4d). The Voronoi scaffolds with 70% porosity exhibited a similar initial deformation behavior to the 60% counterpart. However, after attaining the stress peak, the stress–strain curve entered a sustained plateau stage with minor fluctuations (Figure 4e). The stress–strain curve of the Voronoi scaffold with 80% porosity exhibited a rapid decline after reaching the peak stress (Figure 4f). The V80-200 sample displayed a steep stress plateau, indicating extensive regions of severe and alternating strut fracture, which resulted in an unstable mechanical response. These results suggested that increasing porosity promoted a more unstable deformation behavior in the LPBF-printed Voronoi scaffolds.

The mechanical properties of the LPBF-printed Voronoi scaffolds are shown in Figure 5. The yield strength values of the Voronoi structure with 100 and 400 seeds were similar (Figure 5a), which were 10.35 and 10.12 MPa, respectively. Both were higher than that of the Voronoi scaffold with 800 seeds (8.96 MPa). Similarly, all three Voronoi scaffolds reached the failure at the initial stage of plastic deformation, and the effect of seed density on failure stress mirrored its effect on yield strength. The failure stress of the V70-100 sample (15.03 MPa) was slightly higher than that of the V70-400 sample (14.67 MPa), and both were greater than that of the V70-800 sample (11.84 MPa). These results indicated that higher seed density tended to reduce both yield strength and failure stress. The plateau stress of the V70-100 sample was 10.58 MPa. Due to pronounced fluctuations and a low stress trough during the plateau stage, this value was considerably lower than the corresponding failure stress. In contrast, the V70-400 sample exhibited a higher plateau stress (12.67 MPa) owing to a more stable stress-strain response with reduced fluctuation compared to the V70-100 sample. Similarly, the V70-800 sample achieved a higher plateau stress (11.37 MPa) than V70-100, despite having a much lower yield strength, benefiting from a smoother and more sustained stress plateau stage. This suggested that increased seed density contributed to a relatively higher plateau stress. During the printing process of Voronoi scaffolds by LPBF, formation defects such as those caused by evaporation, adhesion, and unmelted particles occur. An increase in seed density leads to a reduction in the diameter of the struts. The size effect magnifies the influence of these defects on the mechanical properties of the Voronoi scaffold, resulting in a more fluctuating stress plateau for Voronoi scaffolds at high seed densities. The Young's modulus of zinc-based Voronoi scaffolds printed by LPBF across three porosity levels ranged from 0.26 to 0.81 GPa.

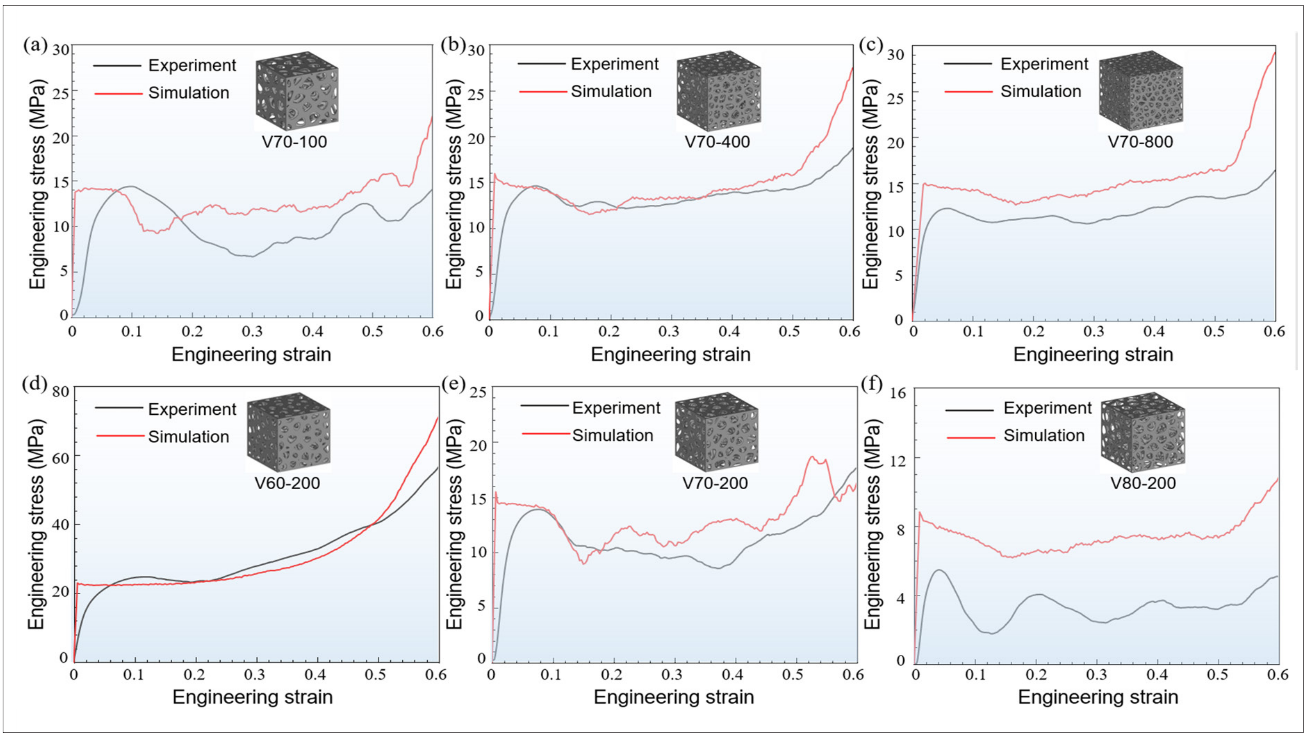

**Figure 4.** Compressive stress–strain curves of Voronoi scaffolds from simulation and experimentation with different seed counts and porosities. (a) V70-100; (b) V70-400; (c) V70-800; (d) V60-200; (e) V70-200; (f) V80-200.

Seed density had minimal impact on the Young's modulus, as values for the different seed configurations remained close (0.53–0.59 GPa). All measured modulus fell within or near the range of trabecular bone (0.462–1.181 GPa),[58-59] indicating potential to mitigate stress shielding after implantation, facilitate stress transfer, and promote bone cell growth. Figure 5b demonstrates the specific energy absorption of Voronoi scaffolds with different seed counts under compression loading. The values were 2.88 J/g for V70-100, 3.06 J/g for V70-400, and 2.67 J/g for V70-800, respectively. Among the three scaffolds, the V70-400 sample achieved the highest energy absorption, due to its yield strength being comparable to that of V70-100 and its higher plateau stress.

The yield strength of the Voronoi scaffold with 60% porosity was 15.87 MPa (Figure 5c), which was higher than those with 70% and 80% porosity. The normalized yield strengths followed the trend: V60-200 (39.69 MPa) > V70-200 (31.23 MPa) > V80-200 (19.2 MPa), indicating that the normalized yield strength increased as the porosity decreased. The three Voronoi scaffolds reached failure at the onset of plastic deformation, with failure stresses of V60-200 (26.35 MPa), V70-200 (13.46 MPa), V80-200 (5.15 MPa), respectively, followed by a transition into the stress plateau stage after the first stress peak. The mechanical properties of the Voronoi scaffolds under different seed densities were normalized to evaluate the influence of the systematic deviation of the actual porosity on the mechanical properties (Figure S1). The results showed that the V70-100 sample with the strongest yield strength exhibited stronger mechanical properties after strength normalization due to its relatively larger actual porosity. The trends of the yield strength and failure stress of the structures under different seed densities remained unchanged. As shown in Figure 5c, the plateau stress for V60-200 was 26.3 MPa, nearly equal to its failure stress due to the minimal stress drop. In contrast, the plateau stress of V70-200 was 10.08 MPa, approximately 25% lower than its failure stress, owing to a more pronounced

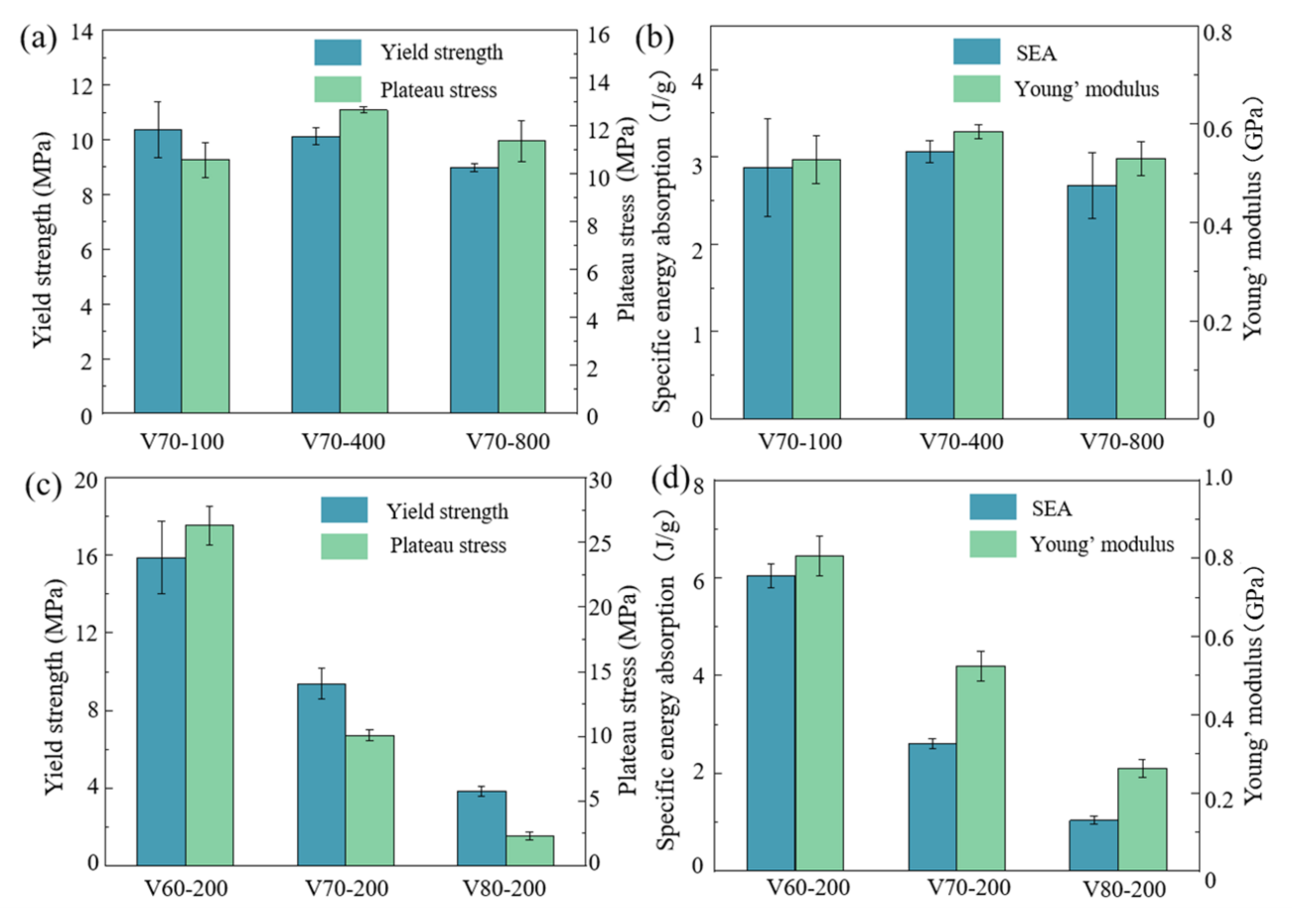

**Figure 5.** Mechanical properties of Voronoi scaffolds printed by LPBF with different seed counts and porosities. (a,c) Yield strength and plateau stress. (b,d) Specific energy absorption and Young's modulus. Abbreviation: LPBF, Laser powder bed fusion.

stress drop. For the 80% porosity scaffold (V80-200), the plateau stress was only 2.29 MPa, significantly lower than its failure stress, attributed to a large-amplitude fluctuation in the stress–strain curve. These results demonstrated that porosity directly affected the plateau stress behavior, with lower porosity scaffolds exhibiting superior plateau stress performance. For energy absorption capacity, the specific energy absorption values of V60-200, V70-200, and V80-200 samples were 6.04, 2.6, and 1.04 J/g, respectively (Figure 5d). Since a stable stress plateau enhanced energy absorption, the higher failure stress and more gradual plateau stage contributed to the significant improved energy absorption and specific energy absorption observed in the V60-200 scaffold.

### 3.3. Deformation behaviors and mechanisms

To analyze the compressive deformation behavior and underlying mechanisms of Voronoi scaffolds with different seed counts and porosities, the stress distribution under small deformations was examined. As shown in Figure 6a, at a constant material volume fraction, a lower seed counts led to fewer struts and a large strut diameter in the V70-100 sample. During loading, each strut consequently bore a higher load compared to those in the V70-400 and V70-800 scaffolds. Therefore, when the load reached a critical threshold, the fracture of any single strut resulted in a more significant reduction in overall structural load-bearing capacity, leading to pronounced fluctuations in the platform stress of the V70-100 sample. Additionally, the large pore diameter reduced strut connectivity, hindering full densification throughout the compression process. In contrast, scaffolds with a higher seed density, such as V70-800, exhibited smaller pores and a denser strut network. Here, fractured struts were more likely to fill adjacent pores and continue contributing to load bearing and transfer, promoting a gradual densification process during compression and a corresponding rise in compressive stress. The V70-800 sample, with its higher seed density, entered the densification stage earlier. In addition, due to its dense strut network and randomly distributed stress concentrations, the V70-800 sample experienced local strut failure at an earlier strain level compared to others. This localized failure initiated a cascading effect, ultimately leading to a lower macroscopic yield strength and an earlier onset of structural failure.

The random distribution of struts in the Voronoi scaffold resulted in nonuniform load transfer during loading, leading to an uneven stress distribution among the struts and causing random occurrences of stress concentration. This uneven stress distribution promoted batch fracture of internal struts as strain increased under compression. Such a failure mode induced fluctuation in the stress plateau, with the extent of deformation directly affecting the amplitude of the stress–strain curve. As shown in Figure 6b, the Voronoi scaffold with 60% porosity exhibited no distinct low-stress regions, with stress predominantly localized on a few struts. In the 70% porosity scaffold, the stress concentration areas expanded, and some low-stress areas appeared at the bottom of the structure. When the porosity increased to 80%, numerous high-stress regions developed within the internal struts. At this stage, significant stress concentration was observed along the upper right boundary of the scaffold, accompanied by bending deformation. The inherent randomness of the Voronoi scaffold led to nonuniform stress distribution, resulting in uncontrolled strut deformation, increased susceptibility to local damage, and thus degraded mechanical performance of the overall scaffold.

The simulation and experimental results of compression deformation characteristics for Voronoi scaffolds with different seed counts under 10%, 30%, and 50% strain are presented in Figure 7. In the V70-100 sample, pores with powder bonding could be observed on the side. At 10% compressive strain, the boundary strut underwent slight bending (Figure 7a), accompanied by a minor rightward tilt of the overall structure. As the strain increased to 30%, the strut in the lower-left corner of the boundary experienced compressive and shear-induced fracture during bending, leading to localized collapse of the pore structure in that region. In addition, surface cracks emerged and the structure exhibited progressive rightward tilting and deformation. The larger strut sizes in the V70-100 sample caused batch failure due to uneven stress distribution, resulting in a significant drop in load-bearing capacity and severe structural deformation. When the strain reached 50%, the internal load imbalance and strut failure triggered global structural instability, manifesting as a ~60° rightward deformation.

In contrast, the higher seed count in the V70-400 sample led to significantly smaller strut diameters compared to V70-100, resulting in lower printing quality. At 30% strain, the bending deformation intensified in the right-side struts, accompanied by the initiation of small surface cracks. The left-side struts experienced shear-induced compression, but the load-bearing capacity remained relatively stable due to limited damage and recontact among struts. Consequently, the deformation process of the V70-400 sample was smoother, which primarily accounted for its more stable stress plateau. When the strain increased to 50%, the bending deformation in the right portion of the scaffold intensified and expanded laterally in combination with crack propagation. On the left side, a local collapse phenomenon was observed due to extensive cracking. At this stage, certain pores were compressed and closed, initiating structural densification. Figure 7c illustrates the compressive deformation process

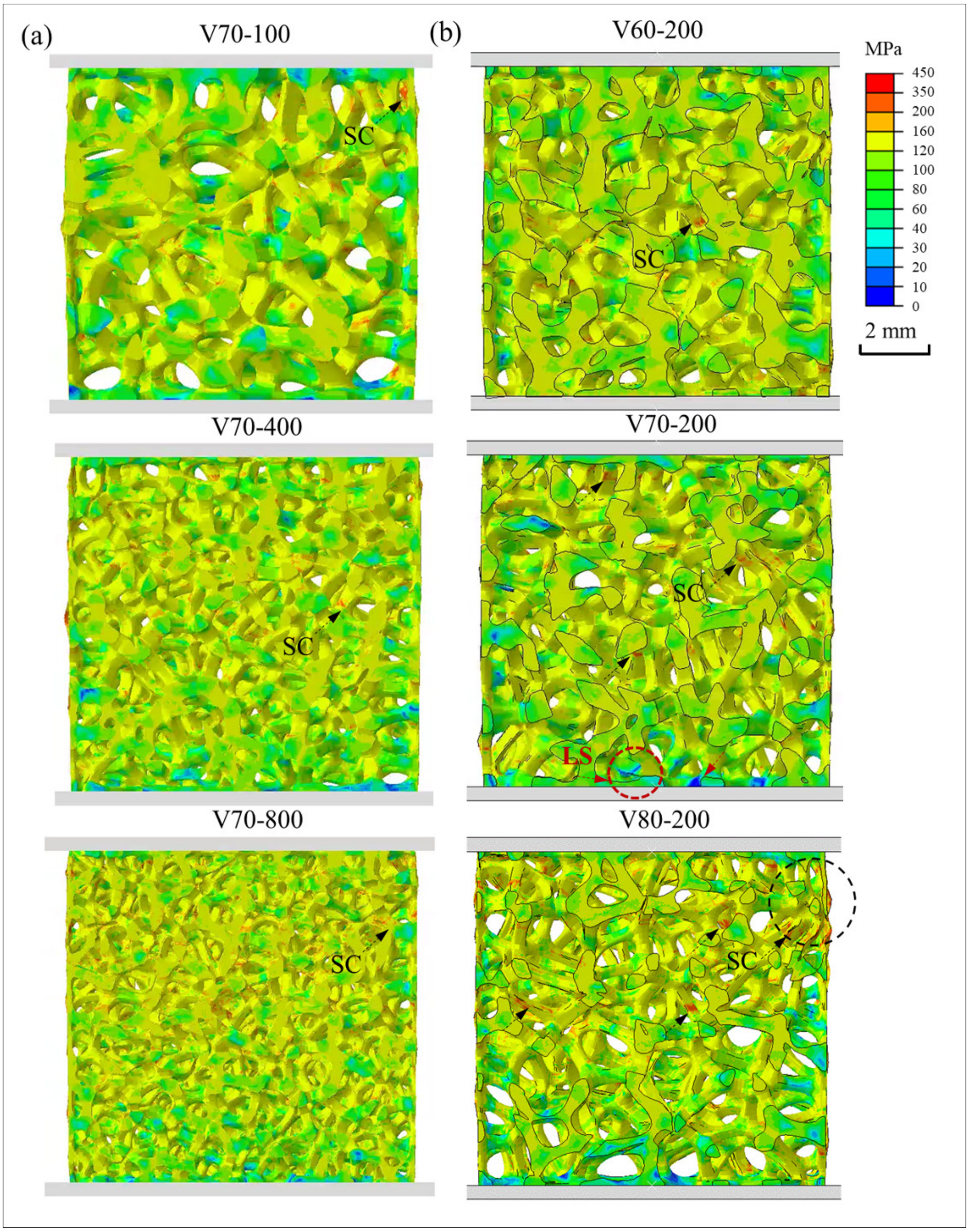

**Figure 6.** Stress distribution of Voronoi scaffolds with different structural parameters under 5% strain. (a) Different seed counts. (b) Different porosity values.

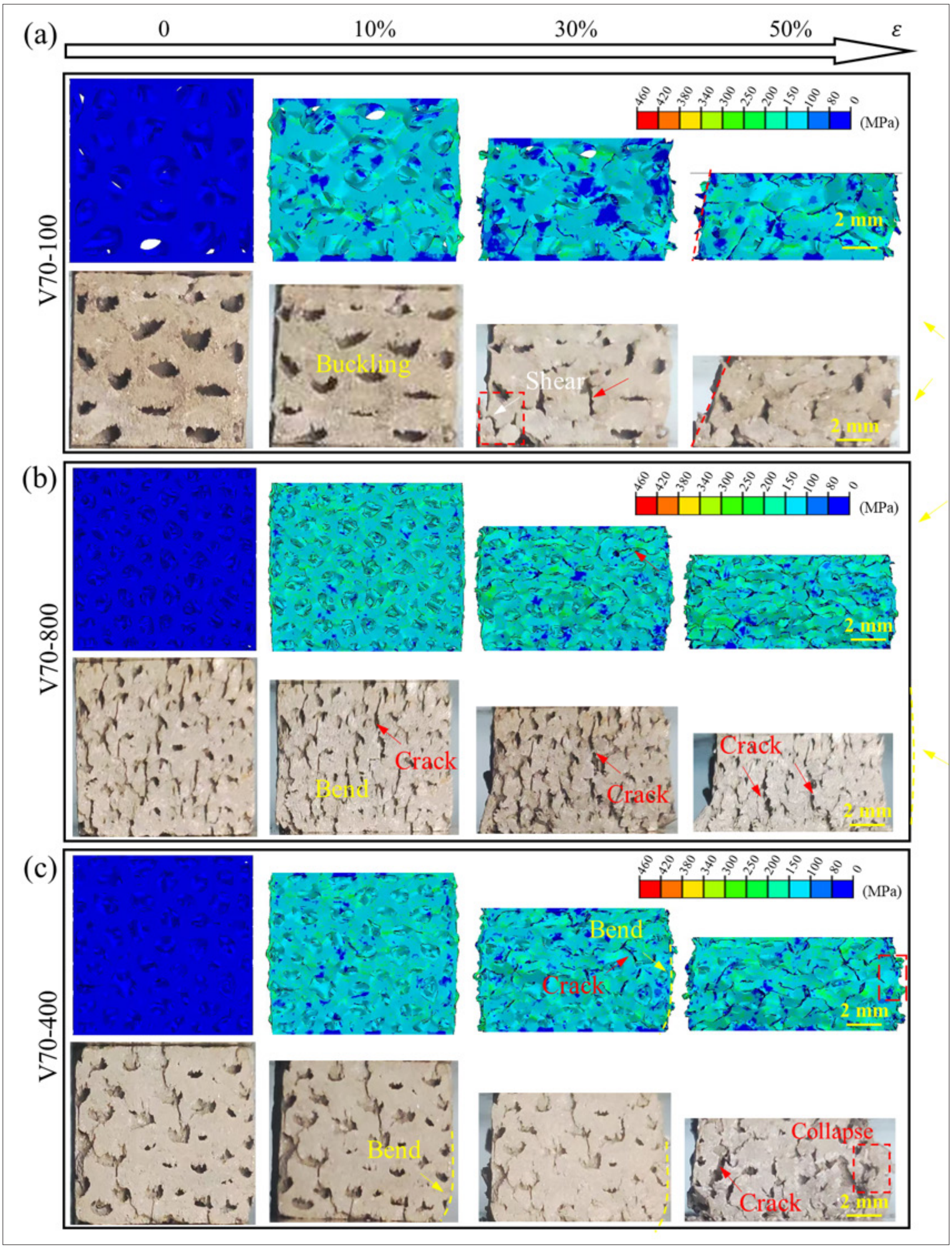

**Figure 7.** Compressive deformation behaviors of Voronoi scaffolds with different seed counts under 10%, 30%, and 50% strain from simulation and experimentation. (a) V70-100; (b) V70-400; (c) V70-800.

of the V70-800 sample. At 10% strain, asymmetric bending deformation occurred on both sides, and the strut fractures led to pore interconnection and the formation of elongated cracks. As the strain increased, bending deformation was aggravated, and crack connectivity extended progressively, forming distinct crack bands that affected the lower layers of the scaffold.

In summary, with the increase in seed density, the number of struts in the Voronoi scaffold also increased. The resulting high-density, randomly distributed struts were more prone to damage, leading to an increase in localized deformation regions with distinct characteristics. The interaction among these regions gave rise to complex deformation modes and reduced the structural load-bearing capacity. However, the dense and random strut distribution mitigated the influence of localized strut failure on the overall mechanical properties, thereby enhancing structural stability during deformation and resulting in higher and more gradual stress plateaus. When the porosity varied, the Voronoi scaffolds with higher porosity exhibited a greater strut length-to-diameter ratio, making them more prone to buckling and fracture under compression. Consequently, at both 70% and 80% porosity levels, the Voronoi scaffolds displayed more pronounced crack band propagation and intensified deformation behavior compared to those at 60% porosity (Figure S2). These differences in deformation directly affected the mechanical response of the scaffolds.

### 3.4. Mass transfer performance

Figure 8 shows the simulation results of pressure drop and permeability fluid dynamics in Voronoi scaffolds. At the same inlet flow rate, the pressure drops for the V70-100, V70-400, and V70-800 scaffolds are 0.381, 0.941, and 1.48 Pa, respectively. As the number of seeds increased, the internal fluid channels in the Voronoi scaffold became more irregularly distributed and geometrically complex, leading to higher flow resistance and reduced permeability. The permeability was inversely correlated with the pressure drop, with a higher seed number guiding lower permeability. Specifically, the permeability of the V70-100 sample ($26.5 \times 10^{-9}$ m$^2$) was 3.9 times greater than that of the V70-800 sample ($6.81 \times 10^{-9}$ m$^2$). Under different porosity levels, the permeability of the V60-200, V70-200, V80-200 scaffolds increased from $10.2 \times 10^{-9}$ to $17.2 \times 10^{-9}$ m$^2$, and finally to $26.1 \times 10^{-9}$ m$^2$. The larger pore volume reduced the fluid flow resistance, thereby enhancing permeability. Due to their trabecular architecture, Voronoi scaffolds with different parameters exhibited permeability values within the reported range for human trabecular bone ($0.75 \times 10^{-9}$ to $7.43 \times 10^{-8}$ m$^2$).[60-61] This similarity supported effective transport of nutrients and metabolic waste in Voronoi-based bone implants during physiological service.

Figure 9 presents the fluid flow pressure and velocity distribution contours of Voronoi scaffolds under different seed counts using CFD simulation. The pressure contour maps revealed a trend that the farther the location from the outlet, the higher the pressure. Comparing the three scaffolds, it is evident that the high connectivity and randomness of fluid channels in these scaffolds resulted in minimal fluctuations in pressure isosurfaces. Within the same height range, Voronoi scaffolds with greater seed counts exhibited higher pressure distributions. Specifically, the overall pressure levels in the V70-100 sample remained below 0.4 Pa, whereas those in the V70-800 sample were significantly higher. This difference arose from the increased internal surface area in the V70-800 sample,

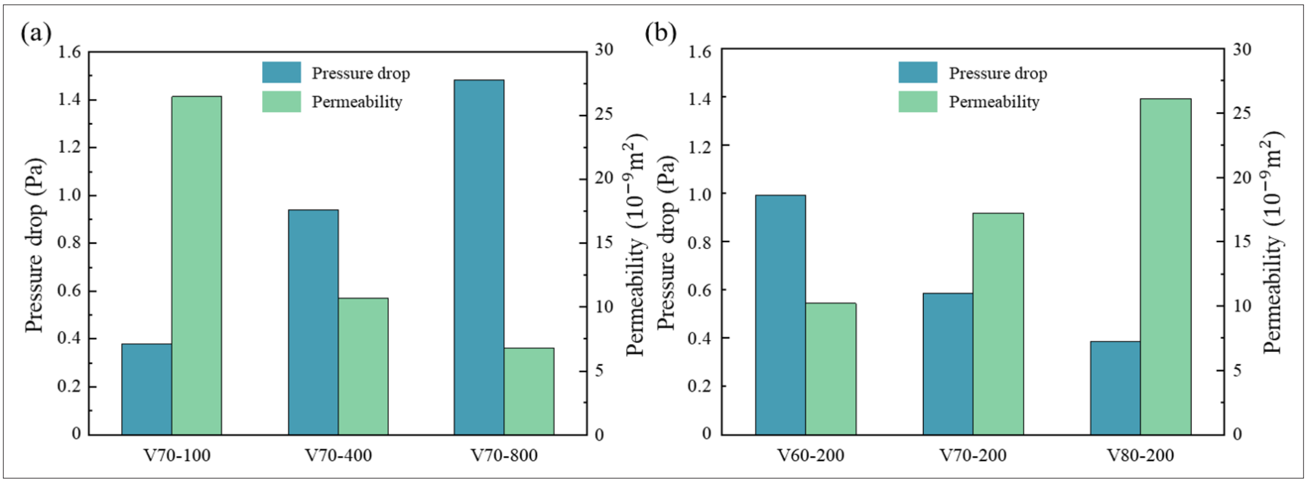

**Figure 8.** Pressure drops and permeability of Voronoi scaffolds from fluid dynamics simulation results. (a) Varying seed counts. (b) Different porosity levels.

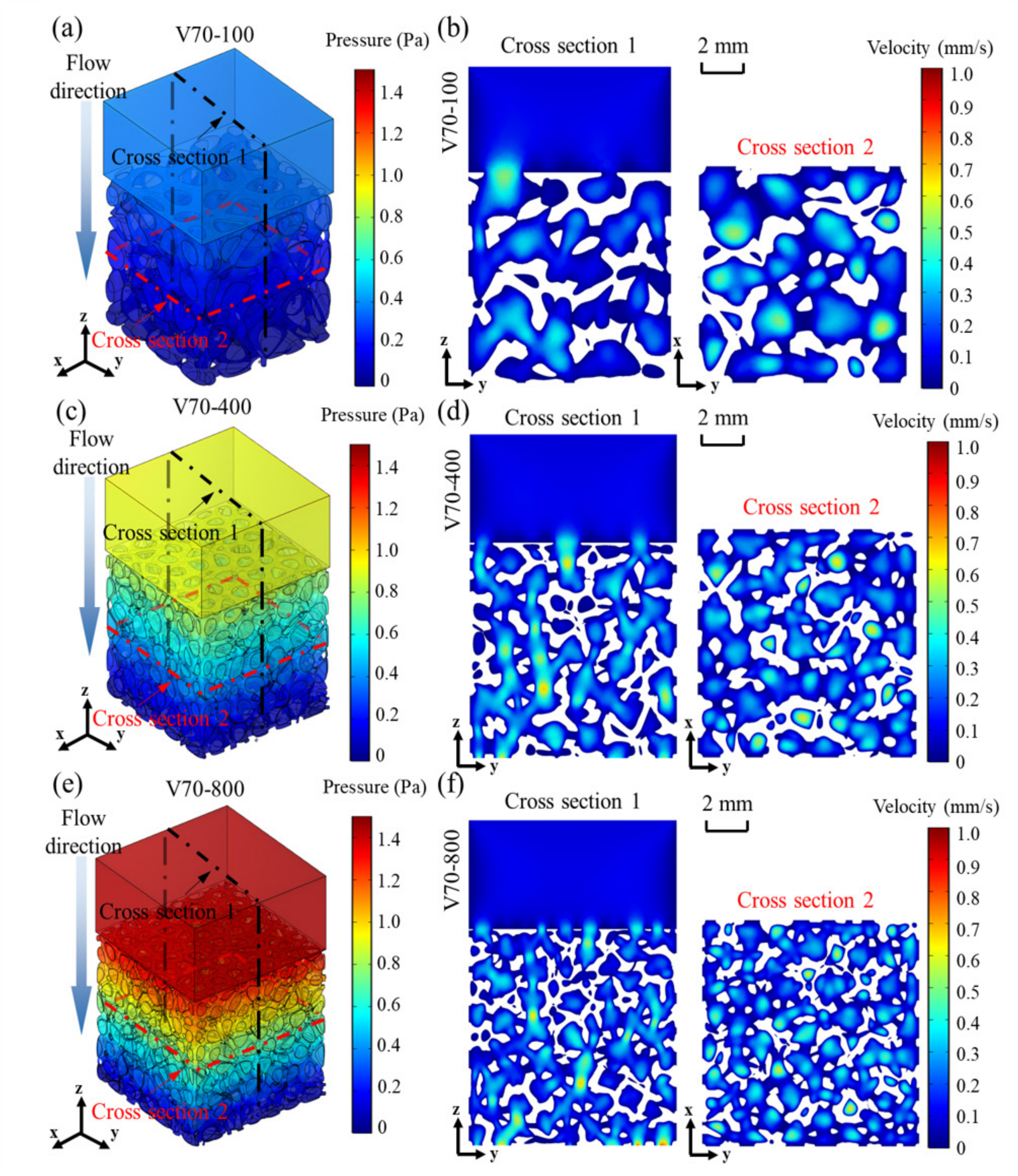

**Figure 9.** Fluid flow analysis of Voronoi scaffolds with different seed counts. (a,c,e) Pressure distribution. (b,d,f) Flow velocity distribution.

which enhanced viscous friction resistance both between the fluid and the solid matrix and among adjacent flow layers within the channels. In addition, the more intricate and staggered flow channels in the V70-800 sample contributed to greater energy dissipation during fluid transport. These factors collectively led to substantial flow energy loss in the V70-800 sample due to its complex fluid channel architecture, thus reducing permeability. Under different porosity levels, reduced pore volume restricted the fluid channels in the Voronoi scaffolds, leading to larger pressure drops and the emergence of localized regions with high flow velocity, which further diminished permeability (Figure S3). Taken together, an increase in both the number and volume of heterogeneous pore channels leads to a greater loss in fluid flow energy.

The mechanical properties and permeability values of the Voronoi scaffolds with different parameters within the reported range of human trabecular bone are similar. Particularly, when compared to the performance of other topological scaffolds (Table S2), the Voronoi scaffolds exhibit properties that are more similar to those of natural cancellous bone. This similarity facilitates the effective transportation of nutrients and metabolic waste by bone implants based on the Voronoi scaffold during biomedical applications and reduces the possibility of stress shielding.

### 3.5. Degradation behaviors

The degradation behavior of zinc-based Voronoi scaffolds not only affects the service life of degradable implants but also influences bone cell growth due to the release of zinc ions during degradation. In this study, *in vitro* degradation experiments were conducted to investigate the degradation behavior of zinc-based Voronoi scaffolds with different structural parameters after 28 days of immersion. To quantitatively compare the degradation rate differences among structures with different seed counts, the weight losses of the V70-100, V70-400, and V70-800 scaffolds after 28 days were measured as 0.153, 0.082, and 0.043 g, respectively. The corresponding degradation rates were calculated as 0.157, 0.056, and 0.027 mm/year, respectively, with the degradation rate of the V70-100 sample being 5.8 times higher than that of the V70-800 sample (Figure 10a). As shown in Figure 10b, zinc-based Voronoi scaffolds with higher porosity exhibited faster degradation rates. Specifically, the degradation rate of the V80-200 sample (0.133 mm/year) was 1.47 times greater than that of the V60-200 sample (0.090 mm/year). These experimental results indicated that increasing the number of seeds significantly reduced the degradation rate of zinc-based Voronoi scaffolds.

To further analyze the degradation behavior of the zinc-based Voronoi scaffolds, SEM imaging was conducted on theirs surfaces after 28 days of immersion in SBF. As zinc ions reacted chemically with inorganic salts and other components in the SBF solution, the elemental composition of the degradation products (such as zinc, oxygen, phosphorus, chlorine, calcium, and carbon elements) was analyzed (Figure 11). A uniform, shell-like corrosion layer formed on the surface of the Voronoi scaffold. At higher magnification, isolated white degradation products were observed on both the surface and edges of this layer (Figure 11a). Around the sample surface and within the surrounding areas, degradation products accumulated in various morphologies, including needle-like, sheet-like, snowflake-like, and shell-like structures. These formations

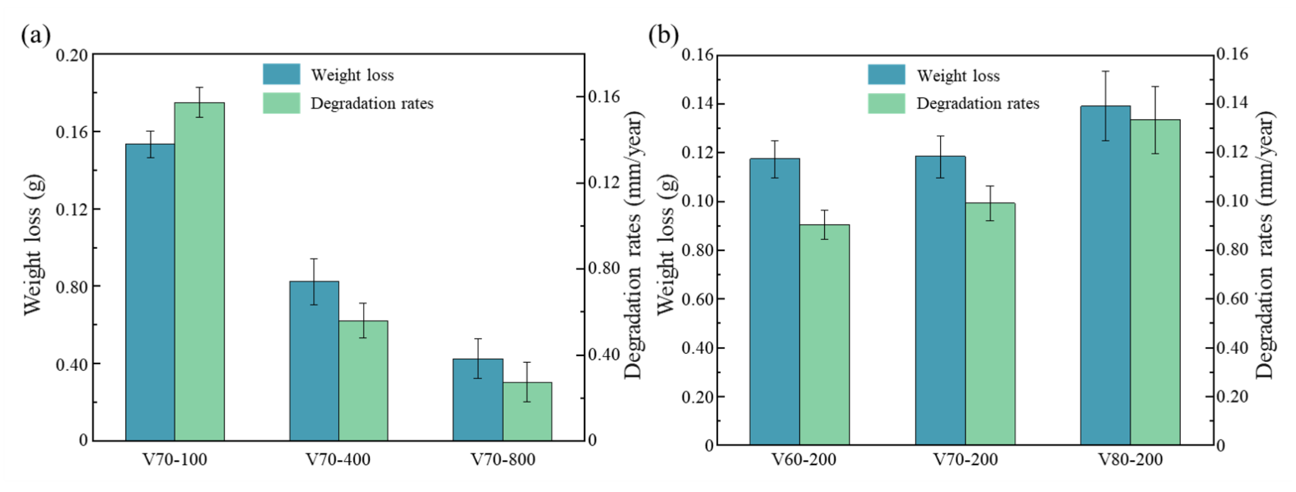

**Figure 10.** Weight loss and permeability of the LPBF-printed zinc-based Voronoi scaffolds: (a) Different seed counts. (b) Different porosity levels. Abbreviation: LPBF, Laser powder bed fusion.

resulted from a series of chemical reactions occurring between zinc and the SBF solution

$$\mathrm{Zn} \rightarrow \mathrm{Zn}^{2+} + 2e^{-}, \tag{XV}$$

$$\mathrm{O}_2 + 2\mathrm{H}_2\mathrm{O} + 4e^{-} \rightarrow 4\mathrm{OH}^{-}, \tag{XVI}$$

$$\mathrm{Zn}^{2+} + 2\mathrm{OH}^{-} \rightarrow \mathrm{Zn(OH)}_2. \tag{XVII}$$

The reduction of $H_2O$ and oxygen produced $OH^-$ ions. As the initial reaction progressed, the accumulation of $OH^-$ ions caused an increase in the pH value. Zinc is more susceptible to passivation, forming $Zn(OH)_2$.[62-63] The $Zn^{2+}$ ions generated at the anode subsequently reacted with other ions and species present in the solution

$$\mathrm{Zn}^{2+} + 2\mathrm{Cl}^{-} \rightarrow \mathrm{ZnCl}_2, \tag{XVIII}$$

$$\begin{aligned} &4\mathrm{Zn(OH)}_2 + \mathrm{ZnCl}_2 + \mathrm{H}_2\mathrm{O} \\ &\rightarrow \mathrm{Zn}_5\mathrm{(OH)}_8\mathrm{Cl}_2 \cdot \mathrm{H}_2\mathrm{O} \end{aligned}. \tag{XIX}$$

The detection of chlorine element in the Voronoi scaffolds after 28 days of degradation was nearly negligible, whereas chlorine distribution was still observable in certain samples after 14 days (Figure S4). This observation might be attributed to the inherent instability of basic zinc chloride ($Zn_5(OH)_8Cl_2{\cdot}H_2O$), which tended to decompose into zinc oxide (ZnO) under alkaline conditions and release $Zn^{2+}$ ions under acidic conditions

$$\mathrm{Zn}_5\mathrm{(OH)}_8\mathrm{Cl}_2 + 2\mathrm{OH}^{-} \rightarrow 5\mathrm{ZnO} + 2\mathrm{Cl}^{-} + 5\mathrm{H}_2\mathrm{O}, \tag{XX}$$

$$\mathrm{Zn}_5\mathrm{(OH)}_8\mathrm{Cl}_2 + 8\mathrm{H}^{+} \rightarrow 5\mathrm{Zn}^{+} + 8\mathrm{H}_2\mathrm{O} + 2\mathrm{Cl}^{-}. \tag{XXI}$$

This led to the predominant presence of chlorine as chloride ions in the solution.[64] Moreover, since SBF contained buffering systems, such as bicarbonate and hydrogen phosphate, dissolved carbon dioxide reacted with $OH^-$ to form $HCO_3^-$, contributing to the formation of a small amount of basic zinc carbonate precipitation

$$\begin{aligned} &5\mathrm{Zn(OH)}_2 + 2\mathrm{HCO}_3^{-} + 2\mathrm{H}^{+} \\ &\rightarrow \mathrm{Zn}_5\mathrm{(CO}_3\mathrm{)}_2\mathrm{(OH)}_6 + 4\mathrm{H}_2\mathrm{O} \end{aligned}, \tag{XXII}$$

$$\begin{aligned} &2\mathrm{HPO}_4^{2-} + 3\mathrm{Zn(OH)}_2 + 4\mathrm{H}^{+} \\ &\rightarrow \mathrm{Zn}_3\mathrm{(PO}_4\mathrm{)}^{2+} + 6\mathrm{H}_2\mathrm{O} \end{aligned} \tag{XXIII}$$

Therefore, the zinc-based Voronoi scaffolds degraded in the SBF solution to form major degradation products, such as ZnO, basic carbonate zinc ($Zn_5(CO_3)_2(OH)_6$), and $Zn_5(OH)_8Cl_2{\cdot}H_2O$. The extensive distribution of P further suggested the potential formation of phosphorous compounds within the degradation layer. The cross-sectional energy-dispersive X-ray spectroscopy (EDS) analysis revealed that the degradation products adhering to the strut surface were rich in zinc and oxygen, while calcium was mainly present in the outer regions of the degradation layer, farther from the strut surface.[65] This indicated that calcium-containing compounds precipitated during the later stages of degradation. Additionally, with prolonged degradation time, these products progressively accumulated and spread outward, leading to the blockage and coverage of pores within the Voronoi scaffold (Figure 10e). As the seed count increased, the interconnected pore channels became increasingly narrower. Under the influence of low permeability, this facilitated further degradation and blockage of internal pores, hindering the diffusion of $Zn^{2+}$ ions and their interaction with SBF, thereby inhibiting the overall degradation process. This mechanism may account for the significant reduction in the degradation rate observed in the V70-800 sample.

### 3.5. Biological activity

Alkaline phosphatase (ALP) is synthesized by osteoblasts and secreted into both the bone matrix and the bloodstream, where it serves as a key enzyme in bone matrix synthesis and mineralization. As shown in Figure S5, ALP staining was employed to evaluate the osteogenic differentiation potential of zinc-based Voronoi scaffolds. ALP expression levels increased over time across all scaffold groups. While variations in porosity had minimal impact on ALP secretion, the seed count significantly affected enzymatic activity. Notably, the V70-800 group exhibited the most intense blue staining and significantly higher ALP activity compared to other groups. Alizarin red staining (ARS) results corroborated these findings: the V70-800 group displayed a substantially greater number of mineralized nodules and the largest ARS-positive area (Figure 12), indicating enhanced extracellular matrix mineralization and calcium deposition. Concurrent cell proliferation assays demonstrated that the zinc-based

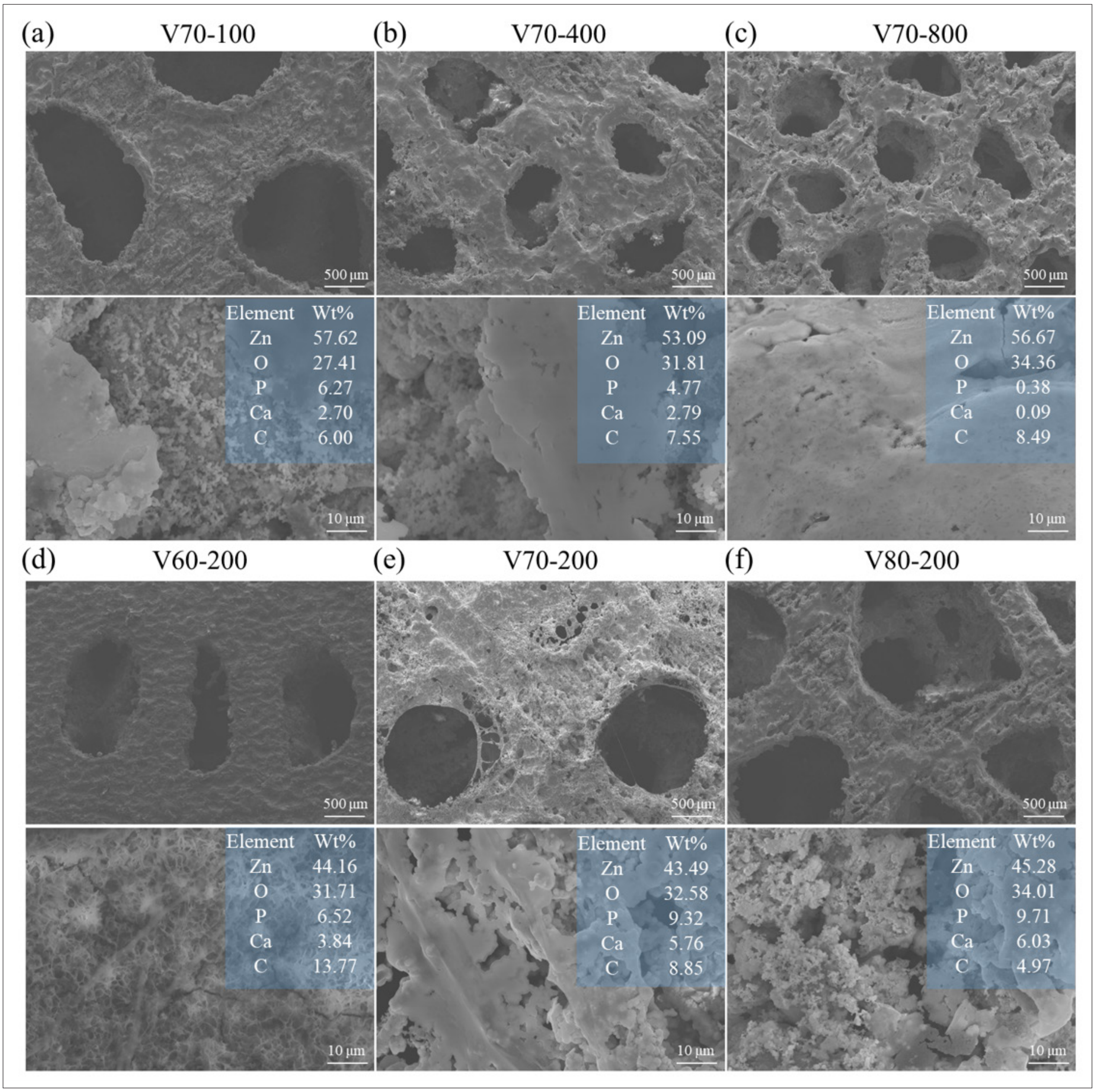

(a) V70-100

| Element | Wt% |
|---|---|
| Zn | 57.62 |
| O | 27.41 |
| P | 6.27 |
| Ca | 2.70 |
| C | 6.00 |

(b) V70-400

| Element | Wt% |
|---|---|
| Zn | 53.09 |
| O | 31.81 |
| P | 4.77 |
| Ca | 2.79 |
| C | 7.55 |

(c) V70-800

| Element | Wt% |
|---|---|
| Zn | 56.67 |
| O | 34.36 |
| P | 0.38 |
| Ca | 0.09 |
| C | 8.49 |

(d) V60-200

| Element | Wt% |
|---|---|
| Zn | 44.16 |
| O | 31.71 |
| P | 6.52 |
| Ca | 3.84 |
| C | 13.77 |

(e) V70-200

| Element | Wt% |
|---|---|
| Zn | 43.49 |
| O | 32.58 |
| P | 9.32 |
| Ca | 5.76 |
| C | 8.85 |

(f) V80-200

| Element | Wt% |
|---|---|
| Zn | 45.28 |
| O | 34.01 |
| P | 9.71 |
| Ca | 6.03 |
| C | 4.97 |

**Figure 11.** Morphology and elemental analysis of LPBF-printed zinc-based Voronoi scaffolds after immersion for 28 days. (a–d) Different seed counts. (e,f) Different porosity levels. Abbreviation: LPBF, Laser powder bed fusion.

Voronoi scaffolds exhibited excellent biocompatibility without obvious cytotoxicity. In the experimental groups with high seed density, increased cell density was observed, along with more favorable cell morphological characteristics (Figure S6). Furthermore, the V70-800 group demonstrated a significant slower degradation rate than other experimental groups. The sustained release of low concentrations of $Zn^{2+}$ from this scaffold promoted osteogenic activity by improving enzyme function without disrupting intracellular metal ion homeostasis or inducing cytotoxicity.

To further investigate the underlying mechanism of the osteogenic differentiation–promoting effect of the zinc-based Voronoi scaffolds, the V70-800 group that exhibited superior osteogenic activity, along with the control group and two additional experimental groups, showed moderately different outcomes. The mRNA expression levels of osteogenic-related key genes, such as type I collagen α1 chain (*COL1*), *ALP*, and osteocalcin (*OCN*), were quantified by means of qRT-PCR to verify and assess the osteoinductive capacity of the scaffolds. As illustrated in Figure 13, all experimental groups exhibited upregulated expression of *COL1* and *ALP* at the mRNA level, with the V70-800 group demonstrating the most robust enhancement. On the day 7, the V70-800 group showed significantly higher expression of both *COL1* and *ALP* compared to the control group, and this difference became more pronounced by the day 14. Notably, *COL1* expression in the V70-800 group reached 4.5-fold that of the control group on the day 14. COL1 facilitated osteoblast adhesion and signaling through specific peptide sequences such as the RGD integrin-binding site and the GFOGER collagen-binding motif, thereby activating downstream pathways that promoted osteogenic differentiation. The zinc-based Voronoi scaffolds effectively stimulated MC3T3-E1 cells to synthesize and secret osteogenic-related proteins. At lower concentrations, $Zn^{2+}$ preferentially enhanced the expression of type I collagen α1 chain, suggesting a targeted regulatory role in early-stage osteogenic differentiation. In summary, adjusting the seed density is a critical determinant for endowing zinc-based Voronoi scaffolds with proliferative and osteoinductive functionalities.

## 4. Conclusion

In this study, the effects of seed count and porosity on the mechanical properties, mass transfer properties, degradation behavior, and osteogenic differentiation of zinc-based Voronoi scaffolds fabricated by LPBF were studied. The main findings are concluded as follows:

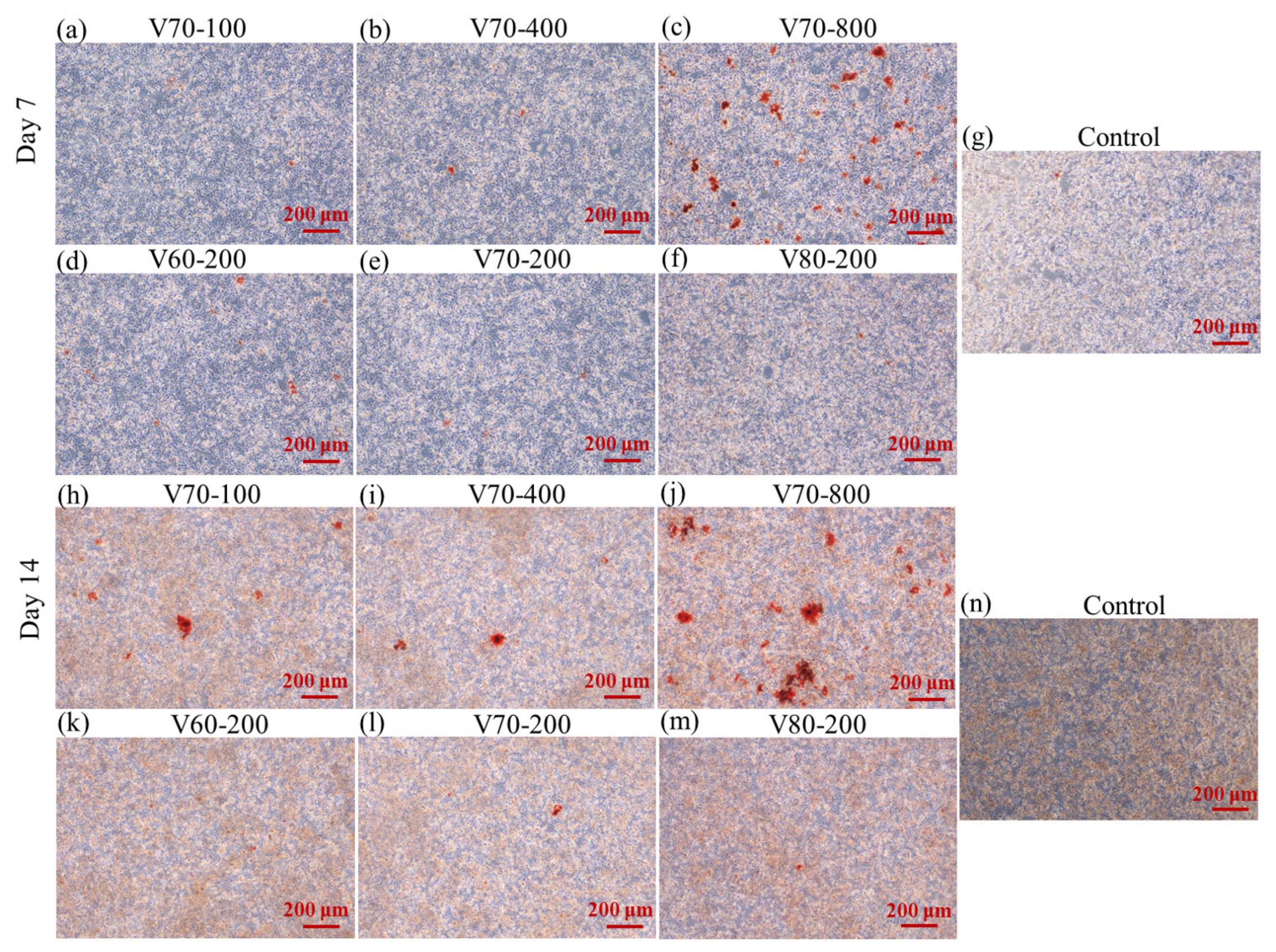

**Figure 12.** Osteogenic differentiation visualized with Alizarin red staining using the 10% extract of the LPBF-printed zinc-based Voronoi scaffolds: (a–g) On day 7. (h–n) On day 14. Abbreviation: LPBF, Laser powder bed fusion.

The influence law of porosity and seed density on Voronoi mechanical properties and deformation mechanism was revealed. The failure and fracture of struts caused by the increase of aspect ratio was the main reason for the decrease of mechanical properties of Voronoi scaffold at a high porosity. The increase of seed density caused more random local strut damage, reduced the structural strength, and reduced the influence of local strut failure on the overall performance of the structure, so as to obtain higher platform stress. Reducing seed counts from 800 to 100 increased the Voronoi scaffold failure stress by 26.9% and decreased the plateau stress by 6.9%.

The permeability of 70% porosity Voronoi scaffolds with different seed counts was in the range of $6.81 \times 10^{-9} - 26.5 \times 10^{-9}$ m$^2$. The permeability of the V70-100 sample ($26.5 \times 10^{-9}$ m$^2$) was 3.9 times higher than that of the V70-800 sample ($6.81 \times 10^{-9}$ m$^2$). Increasing the seed counts boosted the irregular fluid channel inside the Voronoi scaffold, allowing the fluid flow resistance to increase, leading to lower permeability.

The degradation rate of zinc-based Voronoi scaffold decreased with the increase of seed counts, and the degradation rate of V70-100 sample (0.157 mm/year) was 5.8 times that of V70-800 sample (0.027 mm/year). The high number of seeds reduced the connected pore size inside the Voronoi scaffold, and the high pore density and low permeability caused degradation products to deposit more readily and block internal pores, thereby inhibiting $Zn^{2+}$release.

The seed counts in the zinc-based Voronoi structure significantly affected ALP secretion, and the high number of seeds Voronoi scaffold positively regulates extracellular matrix mineralization and calcification by reducing $Zn^{2+}$ release rate. It mainly increased the expression of COL1 and ALP to promote osteogenic differentiation. The expression level of COL1 in the V70-800 group was 4.5 times that of the control group. This work provides a basis for the clinical application of Voronoi scaffolds. However, there are still certain limitations, such as the lack of *in vivo* degradation experiments and long-term degradation research results.

## Acknowledgments

None.

## Funding

This study was supported by the following funds: the Fundamental Research Funds for the Central Universities (No. 2024ZYGXZR079), the National Natural Science Foundation of China (Nos. 52305358 and W2421079), the Young Elite Scientists Sponsorship Program by CAST (No. 2023QNRC001), and the Science and Technology Project of Guangzhou (No. 2025A04J5196).

## Conflict of interest

The authors declare they have no competing interests.

## Author contributions

*Conceptualization:* Boxun Liu, Yunhui Wang, Changjun Han
*Formal analysis:* Boxun Liu, Yunhui Wang, Yi Zhang, Zhengbo Wen, QiXin Liang
*Investigation:* Boxun Liu, Yunhui Wang, Zhi Dong

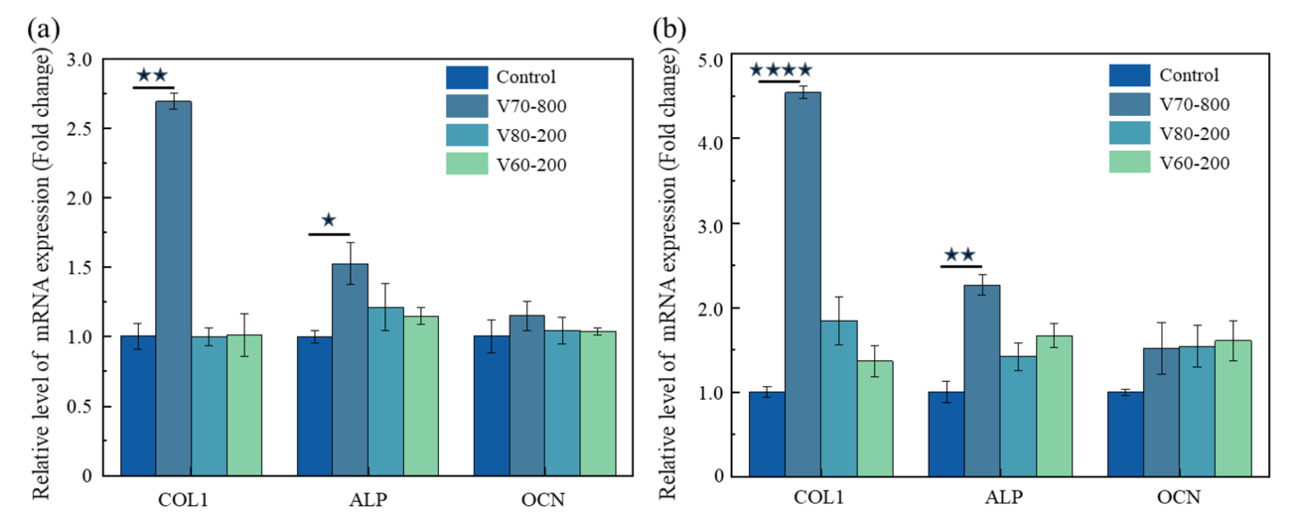

**Figure 13.** Influence of zinc-based Voronoi scaffolds on the relative expression levels of key osteogenic genes COL1, ALP and OCN. (a) On day 7. (b) On day 14.

*Methodology:* Yi Zhang, Zhengbo Wen, QiXin Liang
*Writing–original draft:* Boxun Liu, Yunhui Wang, Yushan Huang
*Writing–review & editing:* Changjun Han, Yunhui Wang, Yushan Huang

## Ethics approval and consent to participate

Not applicable.

## Consent for publication

Not applicable.

## Availability of data

Data are available from the corresponding author upon reasonable request

## References

1. Ling C, Li Q, Zhang Z, *et al*. Influence of heat treatment on microstructure, mechanical and corrosion behavior of WE43 alloy fabricated by laser-beam powder bed fusion. *Int J Extreme Manuf.* 2023;6(1):015001. doi: 10.1088/2631-7990/acfad5
2. Wu X, Liu J, Yang Y, *et al*. Laser powder bed fusion of biodegradable magnesium alloys: process, microstructure and properties. *Int J Extreme Manuf.* 2024;7(2):022007. doi: 10.1088/2631-7990/ad967e
3. Tan C, Zou J, Li S, *et al*. Additive manufacturing of bio-inspired multi-scale hierarchically strengthened lattice structures. *Int J Mach Tools Manuf.* 2021;167:103764. doi: 10.1016/j.ijmachtools.2021.103764
4. Wei S, Ma J, Xu L, *et al*. Biodegradable materials for bone defect repair. *Mil Med Res.* 2020;7(1):54. doi: 10.1186/s40779-020-00280-6
5. Yang Y, Jiang R, Han C, *et al*. Frontiers in laser additive manufacturing technology. *Addit Manuf Front.* 2024;3(4):200160. doi: 10.1016/j.amf.2024.200160
6. Lu Y, Chen G, Long Z, *et al*. Novel 3D-printed prosthetic composite for reconstruction of massive bone defects in lower extremities after malignant tumor resection. *J Bone Oncol.* 2019;16:100220. doi: 10.1016/j.jbo.2019.100220
7. Ran Q, Yang W, Hu Y, *et al*. Osteogenesis of 3D printed porous Ti6Al4V implants with different pore sizes. *J Mech Behav Biomed Mater.* 2018;84:1-11. doi: 10.1016/j.jmbbm.2018.04.010
8. Zhang W, Wang L, Feng Z, *et al*. Research progress on selective laser melting (SLM) of magnesium alloys: a review. *Optik.* 2020;207:163842. doi: 10.1016/j.ijleo.2019.163842
9. Yang M, Yang L, Peng S, *et al*. Laser additive manufacturing of zinc: formation quality, texture, and cell behavior. *Bio-Des Manuf.* 2023;6(2):103-120. doi: 10.1007/s42242-022-00216-0
10. Bandyopadhyay A, Mitra I, Avila JD, *et al*. Porous metal implants: processing, properties, and challenges. *Int J Extreme Manuf.* 2023;5(3):032014. doi: 10.1088/2631-7990/acdd35
11. Gao Z, Ren P, Wang H, *et al*. Additive manufacture of ultrasoft bioinspired metamaterials. *Int J Mach Tools Manuf.* 2024;195:104101. doi: 10.1016/j.ijmachtools.2023.104101
12. Jin J, Wu S, Yang L, *et al*. Ni–Ti multicell interlacing Gyroid lattice structures with ultra-high hyperelastic response fabricated by laser powder bed fusion. *Int J Mach Tools Manuf.* 2024;195:104099. doi: 10.1016/j.ijmachtools.2023.104099
13. Gibson L. The mechanical behaviour of cancellous bone. *J Biomech.* 1985;18(5):317-328. doi: 10.1016/0021-9290(85)90287-8
14. Yang Y, Ling C, Li Y, *et al*. Microstructure development and biodegradation behavior of additively manufactured Mg-Zn-Gd alloy with LPSO structure. *J Mater Sci Technol.* 2023;144:1-14. doi: 10.1016/j.jmst.2022.09.059
15. Gatto ML, Cerqueni G, Groppo R, *et al*. Improved biomechanical behavior of 316L graded scaffolds for bone tissue regeneration produced by laser powder bed fusion. *J Mech Behav Biomed Mater.* 2023;144:105989. doi: 10.1016/j.jmbbm.2023.105989
16. Tyagi SA, Manjaiah M. Additive manufacturing of titanium-based lattice structures for medical applications–a review. *Bioprinting.* 2023;30:e00267. doi: 10.1016/j.bprint.2023.e00267
17. Wang D, Liu L, Tang J, *et al*. Recent advances on additive manufacturing of heterogeneous/gradient metallic materials via laser powder bed fusion. *Int J Extreme Manuf.* 2025;7(6):062007. doi: 10.1088/2631-7990/adf69e
18. Ma S, Tang Q, Han X, *et al*. Manufacturability, mechanical properties, mass-transport properties and biocompatibility of triply periodic minimal surface (TPMS) porous scaffolds fabricated by selective laser melting. *Mater Des.* 2020;195:109034. doi: 10.1016/j.matdes.2020.109034
19. Zhang L, Wang B, Song B, *et al*. 3D printed biomimetic metamaterials with graded porosity and tapering topology for improved cell seeding and bone regeneration. *Bioact Mater.* 2023;25:677-688. doi: 10.1016/j.bioactmat.2022.07.009
20. Fortune S. A sweepline algorithm for Voronoi diagrams. *Proc Second Annu Symp Comput Geom.* 1986:313-322.

doi: 10.1145/10515.10549

21. Du Q, Faber V, Gunzburger M. Centroidal Voronoi tessellations: applications and algorithms. *SIAM Rev.* 1999;41(4):637-676. doi: 10.1137/S0036144599352836
22. Fantini M, Curto M. Interactive design and manufacturing of a Voronoi-based biomimetic bone scaffold for morphological characterization. *Int J Interact Des Manuf.* 2018;12:585-596. doi: 10.1007/s12008-017-0416-x
23. Dong Z, Du H, Xu S, *et al*. Achieving near-isotropic strength and ductility in laser additively manufactured zinc via columnar-to-equiaxed grain transition under thermoelectric magnetic effect. *J Mater Sci Technol.* 2025;258:107-120. doi: 10.1016/j.jmst.2025.09.023
24. Li D, Xie H, Gao C, *et al*. Harmonic heterostructured pure Ti fabricated by laser powder bed fusion for excellent wear resistance via strength-plasticity synergy. *Opto-Electron Adv.* 2025;8(9):250043-1-250043-21. doi: 10.29026/oea.2025.250043
25. Zhao H, Han Y, Pan C, *et al*. Design and mechanical properties verification of gradient Voronoi scaffold for bone tissue engineering. *Micromachines.* 2021;12(6):664. doi: 10.3390/mi12060664
26. Gómez S, Vlad M D, López J, *et al*. Design and properties of 3D scaffolds for bone tissue engineering. *Acta Biomater.* 2016;42:341-350. doi: 10.1016/j.actbio.2016.06.032
27. Herath B, Suresh S, Downing D, *et al*. Mechanical and geometrical study of 3D printed Voronoi scaffold design for large bone defects. *Mater Des.* 2021;212:110224. doi: 10.1021/acsbiomaterials.1c01482
28. Zou S, Gong H, Gao J. Additively Manufactured Multilevel Voronoi-Lattice Scaffolds with Bonelike Mechanical Properties [J]. *ACS Biomater Sci Eng.* 2022;8(7): 3022-3037 doi: 10.1007/s12008-017-0416-x
29. Guaglione F, Caprio L, Previtali B, *et al*. Single point exposure LPBF for the production of biodegradable Zn-alloy lattice structures. *Addit Manuf.* 2021;48:102426. doi: 10.1016/j.addma.2021.102426
30. Xu S, Xue Y, Hu X, *et al*. Relation between materials, process, structure and property of metallic porous bone scaffolds fabricated by laser powder bed fusion (LPBF): a review. *Opt Laser Technol.* 2025;191:113377. doi: 10.1016/j.optlastec.2025.113377
31. Wang H, Shu Z, Chen P, *et al*. Laser powder bed fusion printed poly-ether-ether-ketone/bioactive glass composite scaffolds with dual-scale pores for enhanced osseointegration and bone ingrowth. *Acta Biomater.* 2024;189:605-620. doi: 10.1016/j.actbio.2024.09.055
32. Yang J, Jin X, Gao H, *et al*. Additive manufacturing of trabecular tantalum scaffolds by laser powder bed fusion: mechanical property evaluation and porous structure characterization. *Mater Character.* 2020;170:110694. doi: 10.1016/j.matchar.2020.110694
33. Zhou X, Feng Y, Zhang J, *et al*. Recent advances in additive manufacturing technology for bone tissue engineering scaffolds. *Int J Adv Manuf Technol.* 2020;108(11):3591-606. doi: 10.1007/s00170-020-05444-1
34. Deering J, Dowling KI, Dicecco LA, *et al*. Selective Voronoi tessellation as a method to design anisotropic and biomimetic implants. *J Mech Behav Biomed Mater.* 2021;116:104361. doi: 10.1016/j.jmbbm.2021.104361
35. Duan Y, Du B, Zhao X, *et al*. The cell regularity effects on the compressive responses of additively manufactured Voronoi foams. *Int J Mech Sci.* 2019;164:105151. doi: 10.1016/j.ijmecsci.2019.105151
36. Jiao C, Xie D, He Z, *et al*. Additive manufacturing of Bio-inspired ceramic bone Scaffolds: structural design, mechanical properties and biocompatibility. *Mater Des.* 2022;217:110610. doi: 10.1016/j.matdes.2022.110610
37. Sotomayor OE, Tippur HV. Role of cell regularity and relative density on elastoplastic compression response of 3-D open-cell foam core sandwich structure generated using Voronoi diagrams. *Acta Mater.* 2014;78:301-313. doi: 10.1016/j.actamat.2014.06.051
38. Tang L, Shi X, Zhang L, *et al*. Effects of statistics of cell's size and shape irregularity on mechanical properties of 2D and 3D Voronoi foams. *Acta Mech.* 2014;225(4):1361-1372. doi: 10.1007/s00707-013-1054-4
39. Hou C, Sinico M, Vrancken B, *et al*. Investigation of the laser powder bed fusion manufacturing process and quasi-static behaviour of Ti6Al4V Voronoi structures. *J Mater Process Technol.* 2024;328:118410. doi: 10.1016/j.jmatprotec.2024.118410
40. Wu T, Yu S, Chen D, *et al*. Bionic design, materials and performance of bone tissue scaffolds. *Materials.* 2017;10(10):1187. doi: 10.3390/ma10101187
41. Edelsbrunner H, Seidel R. Voronoi diagrams and arrangements. *Proc First Annu Symp Comput Geom.* 1985:251-262. doi: 10.1145/323233.323266
42. Canny J, Donald B. Simplified Voronoi diagrams. *Proc Third Annu Symp Comput Geom, F.* 1987:153-161. doi: 10.1145/41958.41974
43. Erwig M. The graph Voronoi diagram with applications. *Netw: Int J.* 2000;36(3):156-163. doi: 10.1002/1097-0037(200010)36:3<156::AID-NET2>3.0.CO;2-L

44. Goharian A, Daneshjoo K, Mahdavinejad M, *et al*. Voronoi geometry for building facade to manage direct sunbeams. *J Sustain Archit Civil Eng.* 2022;31(2):109-124. doi: 10.5755/j01.sace.31.2.30800

45. Lazar EA, Lu J, Rycroft CH. Voronoi cell analysis: the shapes of particle systems. *Am J Phys.* 2022;90(6):469-480. doi: 10.1119/5.0087591

46. Sugihara K. Approximation of generalized Voronoi diagrams by ordinary Voronoi diagrams. *CVGIP: Graph Models Image Process.* 1993;55(6):522-531. doi: 10.1006/cgip.1993.1039

47. Han C, Wang Y, Wang Z, *et al*. Enhancing mechanical properties of additively manufactured Voronoi-based architected metamaterials via a lattice-inspired design strategy. *Int J Mach Tools Manuf.* 2024;202:104199. doi: 10.1016/j.ijmachtools.2024.104199

48. Soro N, Attar H, Wu X, *et al*. Investigation of the structure and mechanical properties of additively manufactured Ti-6Al-4V biomedical scaffolds designed with a Schwartz primitive unit-cell. *Mater Sci Eng: A.* 2019;745:195-202. doi: 10.1016/j.msea.2018.12.104

49. Xiao L, Xu X, Feng G, *et al*. Compressive performance and energy absorption of additively manufactured metallic hybrid lattice structures. *Int J Mech Sci.* 2022;219:107093. doi: 10.1016/j.ijmecsci.2022.107093

50. Zhong H, Das R, Gu J, *et al*. Low-density, high-strength metal mechanical metamaterials beyond the Gibson-Ashby model. *Mater Today.* 2023;68:96-107. doi: 10.1016/j.mattod.2023.07.018

51. Fantini M, Curto M, De Crescenzio F. A method to design biomimetic scaffolds for bone tissue engineering based on Voronoi lattices. *Virt Phys Prototyp.* 2016;11(2):77-90. doi: 10.1080/17452759.2016.1172301

52. Dong Z, Han C, Zhao Y, *et al*. Role of heterogenous microstructure and deformation behavior in achieving superior strength-ductility synergy in zinc fabricated via laser powder bed fusion. *Int J Extreme Manuf.* 2024;6(4):045003. doi: 10.1088/2631-7990/ad3929

53. Dong Z, Han C, Liu G, *et al*. Revealing anisotropic mechanisms in mechanical and degradation properties of zinc fabricated by laser powder bed fusion additive manufacturing. *J Mater Sci Technol.* 2025;214:87-104. doi: 10.1016/j.jmst.2024.06.045

54. Syahrom A, Abdul KMR, Abdullah J, *et al*. Permeability studies of artificial and natural cancellous bone structures. *Med Eng Phys.* 2013;35(6):792-799. doi: 10.1016/j.medengphy.2012.08.011

55. Yang Y, Lu C, Shen L, *et al*. In-situ deposition of apatite layer to protect Mg-based composite fabricated via laser additive manufacturing. *J Magnesium Alloys.* 2023;11(2):629-640. doi: 10.1016/j.jma.2021.04.009

56. Wang C, Hu Y, Zhong C, *et al*. Microstructural evolution and mechanical properties of pure Zn fabricated by selective laser melting. *Mater Sci Eng: A.* 2022;846:143276. doi: 10.1016/j.msea.2022.143276

57. Gu D, Zhang H, Dai D, *et al*. Laser additive manufacturing of nano-TiC reinforced Ni-based nanocomposites with tailored microstructure and performance. *Composites, Part B.* 2019;163:585-597. doi: 10.1016/j.compositesb.2018.12.146

58. Maconachie T, Leary M, Lozanovski B, *et al*. SLM lattice structures: properties, performance, applications and challenges. *Mater Des.* 2019;183:108137. doi: 10.1016/j.matdes.2019.108137

59. Gu XN, Zheng YF. A review on magnesium alloys as biodegradable materials. *Front Mater Sci China.* 2010;4(2):111-115. doi: 10.1007/s11706-010-0024-1

60. Grimm MJ, Williams JL. Measurements of permeability in human calcaneal trabecular bone. *J Biomech.* 1997;30(7):743-745. doi: 10.1016/S0021-9290(97)00016-X

61. Zhang L, Wang B, Song B, *et al*. 3D printed biomimetic metamaterials with graded porosity and tapering topology for improved cell seeding and bone regeneration. *Bioact Mater.* 2023;25:677-688. doi: 10.1016/j.bioactmat.2022.07.009

62. Liu L, Meng Y, Volinsky AA, *et al*. Influences of albumin on in vitro corrosion of pure Zn in artificial plasma. *Corros Sci.* 2019;153:341-356. doi: 10.1016/j.corsci.2019.04.003

63. Thomas S, Cole IS, Sridhar M, *et al*. Revisiting zinc passivation in alkaline solutions. *Electrochim Acta.* 2013;97:192-201. doi: 10.1016/j.electacta.2013.03.008

64. Mouanga M, Berçot P, Rauch JY. Comparison of corrosion behaviour of zinc in NaCl and in NaOH solutions. Part I: corrosion layer characterization. *Corros Sci.* 2010;52(12):3984-3992. doi: 10.1016/j.corsci.2010.08.003

65. Qin Y, Liu A, Guo H, *et al*. Additive manufacturing of Zn-Mg alloy porous scaffolds with enhanced osseointegration: in vitro and in vivo studies. *Acta Biomater.* 2022;145:403-415. doi: 10.1016/j.actbio.2022.03.055